Ontogenetic and static allometry in the skull and cranial units of nine-banded armadillos (Cingulata: Dasypodidae: Dasypus novemcinctus)

Kévin Le Verger, Lionel Hautier, Jérémie Bardin, Sylvain Gerber, Frédéric Delsuc, Guillaume Billet

Title:

Ontogenetic and static allometry in the skull and cranial units of nine-banded armadillos (Cingulata: Dasypodidae: *Dasypus novemcinctus*)

Short Running Title:

Cranial allometry in nine-banded armadillos

Authors:

KÉVIN LE VERGER[1*]; LIONEL HAUTIER[2,3] ; JÉRÉMIE BARDIN[4]; SYLVAIN GERBER[5]; FRÉDÉRIC DELSUC[2], and GUILLAUME BILLET[1]

[1] *Museum national d'Histoire naturelle, Centre de Recherche en Paléontologie – Paris, UMR 7207 CR2P MNHN/CNRS/UPMC, Sorbonne Universités, 8 rue Buffon, CP 38, 75005 Paris, France.*

[2] *Institut des Sciences de l'Evolution, Université de Montpellier, UMR 5554 ISEM CNRS/IRD/EPHE, Place Eugène Bataillon, CC65, 34095 Montpellier cedex, France.*

[3] Natural History Museum of London, Department of Life Sciences, Mammal Section, London, United Kingdom.

[4] *Museum national d'Histoire naturelle, Centre de Recherche en Paléontologie – Paris, UMR 7207 CR2P MNHN/CNRS/UPMC, Sorbonne Universités, 4 place Jussieu, 75005 Paris, France.*

[5] *Muséum national d'Histoire naturelle, Institut de Systématique, Évolution, Biodiversité, UMR 7205 ISYEB MNHN/CNRS/UPMC/EPHE, Sorbonne Universités, 45 rue Buffon, CP 50, 75005 Paris, France.*

* Corresponding author: Kévin Le Verger; address: *8 rue Buffon, CP 38, 75005 Paris, France*; telephone number: 01.40.79.53.79; fax number: 01.40.79.35.80. E-mail: kevin.le-verger@edu.mnhn.fr.

ABSTRACT

A large part of extant and past mammalian morphological diversity is related to variation in size through allometric effects. Previous studies suggested that craniofacial allometry is the dominant pattern underlying mammalian skull shape variation, but cranial allometries were rarely characterized within cranial units such as individual bones. Here, we used 3D geometric morphometric methods to study allometric patterns of the whole skull (global) and of cranial units (local) in a postnatal developmental series of nine-banded armadillos (*Dasypus novemcinctus* ssp.). Analyses were conducted at the ontogenetic and static levels, and for successive developmental stages. Our results support craniofacial allometry as the global pattern along with more local allometric trends, such as the relative posterior elongation of the infraorbital canal, the tooth row reduction on the maxillary, and the marked development of nuchal crests on the supraoccipital with increasing skull size. Our study also reports allometric proportions of shape variation varying substantially among cranial units and across ontogenetic stages. The multi-scale approach advocated here allowed unveiling previously unnoticed allometric variations, indicating an untapped complexity of cranial allometric patterns to further explain mammalian morphological evolution.

KEYWORDS: Geometric morphometrics – Shape – Cranial bones – Size variation – Development – Armadillos – Xenarthra – Allometry.

INTRODUCTION

Variation in size is a major component of tetrapod evolution and diversity. Among them, mammals developed a wide range of body sizes since the onset of the Cenozoic era (Smith *et al*., 2010), with multiple independent events of size increase (Baker *et al*., 2015; Bokma *et al*., 2016). The extant mammalian diversity extends over eight orders of magnitude in size (Price & Hopkins, 2015), and this variation has accompanied ecological diversification (Sibly & Brown, 2007; Price & Hopkins, 2015). This size variation was also accompanied with major allometric trends during the course of mammalian evolution, particularly on the skull. Recent studies suggested that craniofacial allometry, i.e. larger faces relative to the rest of the skull in larger individuals, is a general evolutionary trend of morphological change in placentals, and possibly in other groups of vertebrates (Cardini & Polly, 2013; Cardini, 2019; Linde-Medina, 2016). Craniofacial allometry is also observable intraspecifically in developmental series of extant mammals (Cardini & Polly, 2013) but is absent in early diverging amniotes and in stem-mammals such as cynodonts (Hoffman & Rowe, 2018). This shows that the craniofacial allometry might represent a mammal-specific trend at both the evolutionary and ontogenetic levels. Other common allometric aspects previously suggested in the mammalian skull, and generally based on bivariate analyses, include the negative allometry of middle-ear ossicles relative to the skull dimensions (e.g., Nummela, 1995), the negative allometry of the inner ear relative to the petrosal (Billet *et al*., 2015), and more generally the negative allometry of sense organs relative to other skull parts (e.g., Sánchez-Villagra, 2012).

Many recent studies analysed cranial allometry in mammalian species using 3D geometric morphometrics methods (GMM) in relation to functional morphology, phylogeny or cranial integration (Marroig & Cheverud, 2004; Slater & Van Valkenburgh, 2009; Hautier *et al*., 2017; Cardini, 2019). Most of these GMM studies considered the entire skull, and only a few of them touched upon this concept using an atomistic approach, i.e. focusing on more specific anatomical regions. Although it lacks the 3D approach of GMM, the use of linear distances showed on several instances that large cranial regions display different allometries relative to the entire skull (Slijper, 1962; Monteiro *et al*., 1999; Ross & Metzger, 2004; Marroig & Cheverud, 2004). These studies have highlighted complex allometric trends on the mammalian skull, which are likely determined by multiple and interacting developmental processes (Hallgrímsson *et al*., 2019). In fact, much remains to be discovered about these complex morphological patterns especially in the way that allometric growth differentially affects the various parts of the skull and induces cranial shape changes during ontogeny.

Armadillos have been poorly studied regarding allometry despite the fact that the group experienced a spectacular body mass increase in some lineages, especially in glyptodonts (Delsuc *et al*., 2016). The smallest armadillo species do not exceed 0.115 kg while some glyptodonts weighed more than 2,000 kg (Superina & Abba, 2018; Vizcaíno *et al*., 2012). Size was generally treated separately from other biological traits in taxonomic or evolutionary contributions on this group (e.g., Wetzel & Mondolfi, 1979), while other studies addressed allometry in the postcranial skeleton of armadillos from the functional, metabolic or physiological viewpoints (e.g., Frappell *et al*., 1998; Vizcaíno & Milne, 2002; Costa *et al*., 2019). However, Cardini (2019) demonstrated that extant armadillos exhibit a craniofacial evolutionary allometry similar to that of other placental mammals, a trend also detected in a comparative investigation of allometric variations between several armadillo genera (Moeller, 1968) and in two more detailed studies on euphractines (Abba *et al*., 2015) and dasypodines

(Hautier *et al*., 2017). Apart from craniofacial allometry, no other quantitative analysis of cranial allometry exists for armadillos and no cranial shape change related to size was described in the group.

Our study focuses on describing ontogenetic and static allometric patterns in the skull of the most common, best studied, and widely distributed extant cingulate: the nine-banded armadillo (*Dasypus novemcinctus* ssp. Linnaeus, 1758). Being distributed on the two American continents, this taxon can be split in as much as four different geographical morphotypes, some or all of which may represent distinct species or subspecies: Southern, Central, Northern, and Guianan (Billet *et al*., 2017; Hautier *et al*., 2017), as also suggested by molecular studies based on mitochondrial markers (Huchon *et al*., 1999; Gibb *et al*., 2016; Feijó *et al*., 2018, 2019; Arteaga *et al*., 2020). Based on a large sample covering three of these four morphotypes, our study aims at understanding how allometric variation is distributed in their skull and seeks to further characterize the covariation between shape and size across different cranial units, while controlling for potential effects of geography. More precisely, we analysed allometry in: i) the entire skull, and ii) virtually isolated cranial units, looking at both ontogenetic and static allometry. We report heterogeneous cranial allometric patterns in time and space and discuss potential underlying processes.

MATERIAL AND METHODS

SAMPLING

We sampled 96 cranial specimens stored in the collections of the *Muséum national d'Histoire naturelle* (MNHN, *collections Zoologie et Anatomie comparée*, *Mammifères et Oiseaux*) in Paris (France), the Natural History Museum (BMNH) in London (UK), the Museum of Natural Science of the Louisiana State University (LSU) in Baton Rouge (USA), the

American Museum of Natural History (AMNH) in New York (USA), the National Museum of Natural History (NMNH) in Washington (USA) and the *Muséum d'Histoire Naturelle* in Geneva (MHNG, Switzerland) (see Table S1 for a complete list of specimens). The sample is largely similar to that of Hautier *et al.* (2017), although some specimens could not be considered here, as they were too incomplete for the proposed set of landmarks (see below). We also added new specimens to complete the ontogenetic series (details available in Table S1). In order to minimize phylogenetic effects, we did not include specimens belonging to the "Guianan morphotype" (Hautier *et al.*, 2017; Billet *et al.*, 2017) as recent morpho-anatomical and molecular studies considered it to be clearly distinct from other *D. novemcinctus* populations, and to likely represent a new species (Huchon *et al.*, 1999; Gibb *et al.*, 2016; Billet *et al.*, 2017; Hautier *et al.*, 2017; Feijó *et al.*, 2018, 2019; Arteaga *et al.*, 2020). These studies have also shown that other morphotypes recognizable within *D. novemcinctus* may represent sub-species or even distinct species, hence our use of *D. novemcinctus* ssp. to refer to this potential species complex. Pending more definite conclusions on these aspects, the northern, central, and southern morphotypes were included together in our study and their distribution systematically scrutinized within the allometric analyses. In addition, all analyses of ontogenetic allometry were performed on two different datasets for comparison: on the whole sample and on the best-sampled morphotype only (i.e. southern; n = 48). Finally, potential differences between allometric trajectories among morphotypes were also tested. No specimen belonging to the hairy long-nosed armadillo (*Dasypus pilosus*) was included in the study as it is very divergent morphologically, although recent molecular studies have shown that this species may also be part of the *Dasypus novemcinctus* ssp. complex (Gibb *et al.*, 2016; Feijó *et al.*, 2019).

GEOMETRIC MORPHOMETRICS

151 Digital data were acquired using X-ray µCT facilities at the University of Montpellier
152 (France), at the Natural History Museum (BMNH), and at the AST-RX platform of the
153 *Muséum national d'Histoire naturelle* (MNHN). Image stacks were improved in contrast,
154 rotated, cropped, and reduced to 8 bits using the ImageJ software (Schneider *et al*., 2012).
155 Three-dimensional reconstruction and visualization of the skulls and of the virtually isolated
156 bones were performed using stacks of digital images with MIMICS v. 21.0 software (3D
157 Medical Image Processing Software, Materialize, Leuven, Belgium). Cranial shapes were
158 quantified with 131 anatomical landmarks (Fig. 1 and Table 1, 2, S2) placed on the exported
159 3D models using AVIZO v. 9.7.0 software (Visualization Sciences Group, Burlington, MA,
160 USA). The landmarks corresponding to external cranial structures were based on well-
161 established landmark sets from previous studies on mammalian taxa (Goswami & Finarelli,
162 2016; Hautier *et al*., 2017), and new landmarks were added on internal structures. Landmarks
163 were selected to provide a good overall representation of skull shape, isolated bones, and
164 characters traditionally used in cingulate phylogenetic analyses of the group (Gaudin &
165 Wible, 2006; Billet *et al*., 2011). The last criterion was set for future studies aiming at
166 integrating knowledge on allometry and covariation patterns for the construction of
167 phylogenetic characters. All landmarks were positioned on suture contacts or at the maximum
168 of curvature, or extreme points of bony processes, fossae or foramina except for landmark
169 #131 (Fig. 1), which corresponds to the dorsal projection of the most posterior point of the
170 frontal sinuses (see Billet *et al*., 2017) on the midline in dorsal view (it was landmarked with
171 the transparency option in Avizo). This point was added to the landmark set in order to
172 include an anatomical landmark on the large dorsal exposure of the frontal bone. We then
173 performed a generalized Procrustes analysis (Rohlf & Slice, 1990) using function *gpagen* in
174 the R package *geomorph* version 3.1.0 (Adams *et al*., 2019), and intra-individual asymmetries
175 (Klingenberg *et al*., 2002) were removed using the function *symmetrize* in the R package

176 *Morpho* version 2.6 (Schlager, 2017). When some landmarks were missing on one side of the
177 skull, their position was estimated using the function *fixLMmirror* in the *Morpho* R package
178 (see Table S3). The logarithm of the centroid size was used as a size variable for the different
179 cranial structures.
180
181 DETERMINATION OF ONTOGENETIC STAGES
182 The determination of the developmental stage of each specimen was based on dental eruption,
183 cranial ossification and cranial length. Except for size, these variables were each composed of
184 various discrete observations scored numerically. The scored observations were then averaged
185 to be compiled in a dental eruption index and a cranial ossification index. The observations on
186 dental eruption were made on CT-images and on 3D reconstructions of the skulls and
187 corresponded to the number of teeth present, as well as their class and generation. Based on
188 our observations of the upper dentition, we defined five dental stages. Concerning the
189 ossification, only bones whose suture closure vary along our ontogenetic series were scored.
190 The cranial length value (LTC – measure taken between landmarks #1 and #84) used for this
191 analysis was directly sourced from the work of Hautier *et al.* (2017). The combination of
192 these three variables allowed confirming the ontogenetic separation of specimens in five
193 stages. Some specimens could not be allocated to a particular stage because they preserved no
194 teeth. In this case, these specimens were not included in the analyses where information on
195 ontogenetic stage was needed (see Supplementary Information 1, Figs. S1-3, Table S4, S5 for
196 details of the protocol and results concerning the determination of ontogenetic stages).
197
198 ONTOGENETIC AND STATIC ALLOMETRY
199 Only complete specimens (n = 76, Table S1) were included in the analyses of allometry
200 performed on the entire skull (ES). The ES Procrustes alignment was realized on the entire set

of cranial landmarks, including both sides of the skull. For the ES analysis of ontogenetic allometry, the whole sample corresponds to 76 specimens with 48 specimens belonging to the "Southern group", 11 specimens to the "Central group", and 17 specimens to the “Northern group” as defined by Hautier *et al*. (2017) and Billet *et al*. (2017). Only adult specimens were considered in the ES analysis of static allometry (i.e., 51 specimens in total, with 35 from the Southern, five from the Central, and 11 from the Northern groups).

Under the Bone-By-Bone (3B) approach, the analysed objects corresponded to a virtually isolated bone or group of bones that we defined in this study as Operational Bone Units (OBUs). We used the same samples for both the ES and 3B analyses of allometry (n = 76 for ontogenetic allometry; n = 51 for static allometry). Each 3B Procrustes alignment was realized on a reduced set of landmarks corresponding to the OBU under consideration. The allometric component in the shape variation of OBUs was analysed using the skull centroid size as a measure of size. We performed the 3B analyses only on the left cranial side, which was more complete in most cases. These 3B analyses were only performed on one side since many paired bones were not contiguous and to avoid taking into account symmetrized structures (see above). For the 3B analyses, 13 OBUs were defined, including 11 single bones: premaxillary (pmx); maxillary (mx); nasal (na); frontal (fr); lacrimal (lac); jugal (ju); palatine (pal); parietal (pa); squamosal (sq); supraoccipital (so); petrosal (pe). Two OBUs corresponding to bone complexes (alisphenoid-orbitosphenoid-pterygoid-basisphenoid, as-os-pt-bs; basioccipital-exoccipital, bo-eo) were also defined as some of their bony components (alisphenoid-orbitosphenoid; basioccipital-exoccipital) were often fused in adults, and because only OBUs represented by more than three landmarks could be considered. In the whole landmark dataset, only landmark #114 was not included in the 3B approach as it could not be associated with any of the 13 OBUs.

For both the ES and 3B analyses of allometry, we performed a multivariate regression of Procrustes shape coordinates (Izenman, 2013) on size (log Centroid Size) using the function *procD.lm* of the R package *geomorph*. The R^2 (coefficient of determination) of these analyses represents the percentage of the total shape variation explained by the independent variable, here size (Goodall, 1991; Klingenberg & McIntyre, 1998; Drake & Klingenberg, 2008). We referred to this percentage as the "allometric proportion of the total shape variation". We assessed the statistical significance of the regressions against the null hypothesis of isometric variation using permutation tests with 10,000 iterations (Good, 2000). We also present the values for the R^2 of non-significant regressions (at *p-value*>0.05) and comment them cautiously following recent recommendations by Dushoff *et al.* (2019).

COMMON ALLOMETRY AMONG MORPHOTYPES

For the ES approach, differences in allometric trajectories among morphotypes at the ontogenetic and static levels were investigated. For this analysis, we performed a HOS (Homogeneity of Slope Test) using a Procrustes ANOVA (Goodall, 1991) for morphotypes, size, and interaction between both variables (Collyer & Adams, 2013). The HOS performs statistical assessment of the terms in the model using Procrustes distances among specimens, rather than explained covariance matrices among variables, which is equivalent to distance-based ANOVA designs (Anderson, 2001). The HOS calculates the amount of shape variation explained by size, computes the allometric slopes for each category of the independent variable, and quantifies the influence of a given factor on the shape variation. Statistical significance was evaluated with a residual randomization permutation procedure with 10,000 iterations (Collyer *et al.*, 2015). If the null hypothesis of HOS (= parallel slopes) is rejected, then morphotypes differ in their patterns of allometric growth. The HOS analysis was conducted using the *procD.allometry* function of the *geomorph* package version 3.0.7 (Adams

et al., 2018). More precisely, these analyses were performed to identify the interaction between geographic distribution (morphotypes) and allometry on shape variation by including pairwise comparisons between groups (distribution) to assess significant differences of both the direction (angles) and magnitude (amount of change in shape with size) of allometric trajectories. The pairwise comparisons were performed with *advanced.procD.lm* from the *geomorph* package version 3.0.7. When trajectories significantly differed between morphotypes, allometric patterns were analyzed both within the whole sample and within the southern morphotype subsample only.

COMMON ALLOMETRY BETWEEN ONTOGENETIC STAGES

Multivariate regressions of shape on the logarithm of the skull centroid size were also performed for the different ontogenetic stages determined (see Results) in order to compare the allometric proportions between stages for a given OBU. We then tested the allometric differences between each ontogenetic stage for a given OBU. This preliminary investigation could not be conducted within particular morphotypes because their sampling per ontogenetic stage for each was too low. For this analysis, we performed also a HOS test using a Procrustes ANOVA on each OBU for ontogenetic stage, size, and interaction between both variables. In order to reduce biases linked to sample size, we calculated the angles of each slope for a given OBU versus the horizontal axis to test whether the different ontogenetic stages for a given OBU share a common allometry (see Klingenberg, 2016). The ratio between the OBU relative size and its average for a given ontogenetic stage was also calculated for each stage and for the entire sample in order to analyse the growth dynamics of the OBU.

RESULTS

ALLOMETRY AND GEOGRAPHY

The regression of shape on log centroid size in our ontogenetic series of *D. novemcinctus* ssp. accounts for 27.62% of the total shape variation (*p-value* < 0.0001, Figs. 2; S4). The geographical distribution explains 16.64% of the total shape variation (*p-value* < 0.0001, Fig. S4). At the ontogenetic level, the morphotypes show a slight difference in their allometric trajectory attesting to an interaction between geography and allometry on shape variation during ontogeny (Fig. S4). However, this effect seems to be minimal (3.16 %; Fig. S4). The HOS test pairwise comparisons of ontogenetic allometric trajectories suggests no difference between the Central and Southern morphotypes, but a significant difference between the latter two and the Northern morphotype. These results should be taken with caution as the *p-value* is very close to the statistically significance threshold in the comparison between the Central and Southern morphotypes (= 0.0515) and the difference revealed with the Northern morphotype may be due to the lack of specimens as young as for the other two morphotypes. Because these results suggest that the ontogenetic allometries may slightly differ among morphotypes, the allometric shape changes during ontogeny were analyzed both within the whole sample (see below) and within the Southern morphotype subsample (Fig. S5).

The regression of shape on the logarithm of the centroid size in our adult sample of *D. novemcinctus* ssp. accounts for only 6.31% of the total shape variation (*p-value* < 0.0001, Figs. 2; S4). The effect of geographical distribution is proportionally higher, expressing 22.81% of the total shape variation (*p-value* < 0.0001, Fig. S4). At the static level, the morphotypes share a common allometric trajectory and no interaction between geography and allometry is statistically supported, although the *p-value* is close to the significance threshold (*p-value* = 0.0619). It should also be noted that the central morphotype has relatively low sample size (Fig. S4). The HOS test pairwise comparisons of static allometric trajectories suggests no difference between each morphotype. Because these results suggest that the static

allometries are similar among morphotypes, the allometric shape changes at the adult stage were analyzed within the whole sample only (see below).

ALLOMETRIC VARIATIONS ON THE ENTIRE SKULL (ES)

Ontogenetic allometry

Three main regional trends of skull allometric variation can be recognized in our ontogenetic series. Adult cranial proportions clearly differed from juvenile ones in the relative size of the snout and zygomatic arches compared to the braincase (Fig. 2A; Table S6). The snout undergoes an anteroposterior elongation with size increase. This elongation is bidirectional (one directed anteriorly and the other posteriorly) and has different magnitudes of variation depending on the landmarks considered. Most of the landmarks of the anterior tip of the snout (#1; #3-20) and the ones delineating the posterior end of the premolar row (#29-30), show an anterior displacement relative to other landmarks during growth. On the other hand, most landmarks of the snout posterior to the premaxillary and nasal display a posterior directed elongation relative to the other landmarks. In addition to this elongation, the posterior end of the snout (i.e., delimited anteriorly by the most anterior point of the zygomatic arches) narrows in larger specimens, especially at the level of the infra-orbital and maxillary foramina. The zygomatic arches extend more ventrally and the temporal fenestra widen considerably as the size increases, as expressed by the vectors associated to landmarks #22-23 and #51-52, and by the increase of the post-orbital constriction (#41-42). In the posterior half of the skull, most of landmark displacements are directed towards the centre of the braincase. During ontogeny, the proportions of the neurocranium decreases relative to the rest of the skull due to allometric growth. More local allometric changes are also highlighted: the landmark located at the posterior edge of the frontal sinuses (#131) is particularly distinctive for its strong relative posterior displacement. The dental row is relatively shorter in larger

specimens, with an anterior displacement of the posterior portion of the dental row (#29-30) while the anterior portion varies very slightly (#27-28). The analysis of the ES ontogenetic allometry in the southern morphotype revealed remarkably similar shape changes to the ones described above (Fig. S5).

Static allometry

An increase in size, at the static level, is only associated with minor shape variations of the skull (Fig. 2B; Table S6), similar to the pattern detected with the ontogenetic analyses of allometry, albeit to a lesser degree and with some variations specific to this level (see below). The most anterior part of the nasal bone shows a relative anterior displacement, just like the W-shaped processes in front of the premaxillary (as defined by landmarks #8; #11-14; Fig. 1). The rest of the face shows a relative narrowing as size increases. The shape changes of the zygomatic arches (slightly increasing width) are less strong than in the ontogenetic allometry analyses. The reduction in the relative proportions of the braincase is more pronounced for landmarks located on the cranial roof (frontal and parietal midline landmarks (#113; #114; #131)) and the zygomatic-pterygoid region. The anterior border of the orbit widens as the post-orbital constriction becomes stronger with size. Strikingly, the landmark located on the maxillary-palatine suture (#21) strongly moves forward in comparison to other surrounding landmarks as size increases, much more than in the ontogenetic analysis. A very strong anterior (#19-21; #45-46) and weak posterior (#32) relative elongation of the palatine is detected at the static level. For all other landmarks, the allometric changes appear very weak when compared to their changes in the analysis of ontogenetic allometry.

ALLOMETRIC VARIATIONS STUDIED BONE BY BONE (3B)

Comparison between OBUs

We observe differences in the proportions of allometric shape variation between different OBUs both at the ontogenetic and static levels. In both cases (Fig. 3), the regression of shape on size shows no statistical support for the lacrimal (Fig. 3; Table 3; Figs. S6-7). This is not the case for other OBUs, for which at least the analyses at the ontogenetic level show a significant allometric effect. At the ontogenetic level, the premaxillary has the lowest proportion of shape variation explained by size of all OBUs (lacrimal excluded; Fig. 3A and Table 3). The jugal, petrosal, parietal, as-os-pt-bs OBU, nasal, palatine have a proportion of shape variation explained by size varying between 5% and 10% (Fig. 3A and Table 3). The maxillary, supraoccipital and squamosal show allometric proportions between 10% and 12% (Fig. 3A and Table 3). Finally, the last two OBUs showing the highest proportion of variation explained by size at the ontogenetic level are the bo-eo OBU and the frontal, the latter with more than twice the proportion values find in the other OBUs (Fig. 3A and Table 3). At the static level, the allometric proportion is much lower than at the ontogenetic level for most OBUs. Only five OBUs show a statistically well-supported allometric effect at this level. Among them, the petrosal and the as-os-pt-bs OBU show an allometric proportion lower than 5% (Fig. 3B and Table 3). The frontal shows a drastic reduction in its allometric proportion (5.96%) (Fig. 3B and Table 3). Finally, the parietal and palatine have an allometric proportion almost equivalent to that obtained at the ontogenetic level – for the palatine, it is even higher to that of the entire skull (Fig. 3B and Table 3).

All descriptions of the allometric shape changes below describe the maximal shapes as compared to the minimal shapes per OBU at the ontogenetic level. This was done only for the OBUs whose allometric variation is statistically well-supported (*p-value* < 0.05). Only landmarks on the left side of the skull are mentioned (see Table 1 and Table 2 for their symmetrical landmark/counterparts). The same analyses were performed using the Southern

morphotype only. We obtained very similar results (Fig. S5) as the ones described hereafter for the entire dataset. The only notable differences are generally in the norm (i.e. lesser) of the vectors and not in their direction. The results and shape changes explained by size for the static level on the whole sample are illustrated in Fig. S8 and those changes that differ from the ontogenetic level are described in Supplementary Information 2.

Alisphenoid-Orbitosphenoid-Pterygoid-Basisphenoid complex (Fig. 4A1-A3)

When the skull size increases, the foramen ovale (#70) shows very little variation, while the transverse canal foramen (#68) takes a more medial position. The pterygoid wings (#66) are more extended posteriorly. The optical foramen is located more dorsolaterally (#75). Internally, the most lateral point of the dorsal transverse ridge (#130), which delimits the ethmoidal fossa anteriorly, is more laterally positioned. Finally, the contact between the frontal, the squamosal, and the alisphenoid (#44) is located much more anteromedially.

Basioccipital-Exoccipital complex (Fig. 4B1-B3)

As size increases, the basioccipital becomes mediolaterally wider (#90). The concavity that constitutes the posterior part of the jugular foramen is less marked (#96). The occipital condyles are relatively larger and more anterolaterally oriented (#92; #100). The foramen magnum (#92; #101) is relatively narrower mediolaterally, its ventral portion being more ventral. The exoccipital meets the supraoccipital much further dorsoanteriorly (#94).

Frontal (Fig. 4C1-C3)

The allometric changes mainly involve the posterior development of the frontal sinuses (#131), the deepening of the post-orbital constriction (#42), and a more posteroventral location of the ventral intersection of the annular ring and cribriform plate (#113). While the

400 frontal sinuses are poorly developed in the juvenile stage, they extend much farther
401 posteriorly in older specimens (see also Billet *et al.*, 2017). The anterior part of the frontal
402 extends further anteriorly in larger individuals (#2; #34; #36) while its posterior part is
403 relatively shortened anteroposteriorly and compressed dorsoventrally, as expressed by the
404 landmarks #44, #78, and #81. Finally, the anterior edge of the orbit is placed only slightly
405 more medially (#38).
406
407 *Jugal (Fig. 4D1-D3)*
408 Two main allometric trends can be recognized for the jugal. Its anterior part, in contact with
409 the lacrimal and the maxillary (#50), shows a relative shortening as size increases. The second
410 trend corresponds to a dorsoventral increase of the zygomatic arch (#23; #54; #56), which is
411 stronger in its anteroventral and posterodorsal parts.
412
413 *Maxillary (Fig. 4E1-E3)*
414 From the juvenile stage to the adult stage, the maxillary shows a relative anterior elongation
415 as shown by the landmarks in contact with the premaxillary (#4; #5; #7), especially ventrally
416 at the level of the midline. The landmarks in contact with the palatine (#19; #21) are shifted
417 anterodorsally and the dorsal part of the snout (#34; #36) more posteroventrally. While the
418 maxillary is bulging in its dorsal mid-part in juveniles, it is much shorter dorsoventrally in
419 larger specimens, as marked by the landmark in contact with the nasal and the frontal (#34).
420 Large specimens also display a proportionally reduced dental row (#29; #31). The zygomatic
421 process of the maxillary shows a more ventrolateral position (#23). Finally, the relative length
422 of the infraorbital canal varies strongly from juveniles to adults, the maxillary foramen being
423 more posterior in larger specimens, as expressed by the landmark #25.
424

425 *Nasal (Fig. 4F1-F3)*

426 The nasal is relatively narrower mediolaterally in larger specimens with a much more
427 pronounced internal curvature. Only the landmarks in contact with the premaxillary (#4; #10)
428 show a slight anterior elongation in the medial part of the bone.

429

430 *Palatine (Fig. 5G1-G3)*

431 The palatine becomes relatively more elongated anteroposteriorly and narrower
432 mediolaterally as size increases. This elongation is particularly visible between the
433 anterolateral edge of the palatine and the caudal palatine foramen that became more distant
434 from one another as size increases (#19; #21; #46).

435

436 *Parietal (Fig. 5H1-H3)*

437 The parietal is slightly more elongated anteroposteriorly and narrower mediolaterally in larger
438 specimens (#78; #79; #81; #83). The tentorial process forms a higher ventrally-directed crest
439 as size increases (#73).

440

441 *Petrosal (Fig. 5I1-I3)*

442 On the promontorium, size has little effect on shape variation except at the anterior and
443 medial borders, which are slightly more reduced as size increases (#104; #124). In larger
444 specimens, the mastoid process (#106) is much more pronounced ventrally, the dorsal tip of
445 the crista petrosa (#118) is more anterodorsal, and the bottom of the fossa subarcuata shows a
446 relatively more posterior position (#126).

447

448 *Premaxillary (Fig. 5J1-J3)*

449 The premaxillary is slightly more elongated dorsally in larger specimens while the situation is
450 more complex ventrally. Medially, the premaxillary shortens (#5; #8) while it elongates
451 laterally (#7; #14). The W-shaped process located in the anterior part of the bone (Fig. 1) is
452 more pronounced laterally with a deeper curvature (#12) and longer processes (#14).
453 However, the W-shaped process is less sharp medially as its midline point is positioned more
454 posteriorly (#8). The incisive foramen becomes relatively shorter anteroposteriorly mainly
455 due to the anterior displacement of the most posterior point of these foramina (#18).
456
457 *Squamosal (Fig. 5K1-K3)*
458 The relative allometric reduction of the braincase is also visible on the dorsal edge of the
459 squamosal of larger specimens (#81; #83). As for the jugal, we observe a dorsoventral
460 increase of the zygomatic process of the squamosal (#54; #56). The posterior root of the
461 zygomatic arch (#62) is also relatively more posterior. The posterior opening of the
462 posttemporal canal (Gaudin & Wible, 2006) is more dorsal in larger specimens (#88). The
463 postglenoid process (#58) is more pronounced anterolaterally and the postglenoid foramen
464 (#60) is positioned slightly more medially. Therefore, the postglenoid process and postglenoid
465 foramen are relatively more distant from one another on larger skulls. The sulcus for the
466 external acoustic meatus (#64) is shallower and positioned more medially in larger specimens.
467 Finally, the most posteroventral point between the alisphenoid and squamosal (#72) and the
468 tip of the entoglenoid (#77) are shifted posteriorly.
469
470 *Supraoccipital (Fig. 5L1-L3)*
471 The increase in size is accompanied by a slight lateromedial narrowing (#83) and a
472 dorsoventral elongation (#102) of the supraoccipital. The processes of the nuchal crests
473 undergo a strong posteromedial development in larger specimens (#86). The external occipital

474 crest (#84) is less prominent. In the inner part of the supraoccipital, the lateral occipital
475 vertical ridges (#116) are more developed in the anterior part of the caudal cerebral fossa.
476
477 ## ALLOMETRY AT DIFFERENT STAGES
478 The allometric proportion of shape variation varies between the juvenile, subadult, and adult
479 stages for a given OBU and for the entire skull in the whole sample (Fig. 6A; Table 4; Table
480 S7). For the entire skull, the allometric proportion decreases from juvenile to adult stages. In
481 the 3B approach, the stage with the highest allometric proportion of shape variation varies
482 from one OBU to another. The juvenile stage shows the highest allometric proportion for the
483 maxillary, the frontal, the basioccipital-exoccipital complex, and the petrosal (Fig. 6A; Table
484 4; Table S7). Allometric effects are often not statistically supported in older stages for these
485 OBUs, as exemplified by the bo-eo OBU that only shows a strongly supported allometric
486 effect at the juvenile stage. The allometric proportion of the maxillary shape variation in
487 juveniles is only slightly higher than that retrieved at the subadult stage. The subadult stage
488 shows the highest allometric proportion for the premaxillary, lacrimal, jugal, palatine,
489 parietal, squamosal, and supraoccipital (Fig. 6A; Table 4; Table S7). Allometric effects are
490 statistically supported only at the subadult stage for the lacrimal, jugal, premaxillary,
491 squamosal, and supraoccipital among these OBUs. The allometric proportion of shape
492 variation is generally very low at the adult stage. The frontal, palatine, parietal, as-os-pt-bs
493 OBU, and petrosal all display allometry at this stage (Fig. 6A; Table 4; Table S7). The nasal
494 bone is the only OBU that shows no stage with a supported static allometry. Stages with the
495 highest allometric proportion for a given OBU generally show a higher slope (Table 4). Thus,
496 the subadult stage is usually characterized by the highest slope coefficients for most OBUs.
497 The comparison of the angles of each regression slope with respect to the horizontal
498 axis shows that several OBU stages may share a common allometry (Fig. S9, Table 4, Table

S7-8). By cross-checking these results with the statistical support values obtained for the allometric analyses of a given OBU at a given stage (Table 4 and Fig. 6A), we find that only the juvenile and subadult stages of the maxillary (for which the angles are negative) and the juvenile and adult stages of the petrosal show a common allometry in our sample. This analysis also reveals a significantly different allometric effect between the subadult and adult stages of the palatine and parietal. (Fig. S9, Table 4, Table S7-8).

SIZE VARIATION PER OBU AND ALLOMETRY

The variation in size of an OBU relative to its mean size is different from one OBU to another and among ontogenetic stages (Fig. 6B). At the juvenile stage, the OBUs with the largest size variations from their mean are the maxillary, nasal, lacrimal, jugal, palatine, squamosal, supraoccipital, and bo-eo OBUs. At the subadult level, OBUs with the largest variation in size constitute the anterior part of the snout (i.e., premaxillary, maxillary, and nasal). In the adult stage, the OBUs with the greatest variation in size from their mean correspond to the lacrimal, jugal, and palatine. Finally, over the entire sample and stages, the size variation of an OBU compared to its average size enables us to sort the OBUs into two categories: those with a large size range (i.e., premaxillary, maxillary, nasal, frontal, lacrimal, jugal, and palatine) and those with a small size range (i.e., parietal, squamosal, as-os-pt-bs OBU, supraoccipital, bo-eo OBU, and petrosal) (Fig. 6B). These patterns of size variation do not reflect the allometric proportions per OBU and per stage. However, the two size categories clearly separate an anterior from a posterior block of OBUs, which recall the allometric pattern detected on the entire skull (Fig. 2 and see Discussion).

DISCUSSION

ALLOMETRIC AND GEOGRAPHICAL INTERACTION

In mammals with a wide geographical distribution, such as the Pan-American nine-banded armadillos, allometric patterns can vary with geography and across environments (e.g., Meloro *et al*. 2014; Bubadué *et al*. 2015; Ferreira-Cardoso *et al*., 2019). Recent work on nine-banded armadillos has shown that variation in cranial shape had an important geographic imprint in this widely distributed species (Hautier *et al*., 2017). In conjunction with evidence from internal anatomy and molecular data, these observations suggested the existence of four morphotypes (Southern, Central, Northern and Guianan) that potentially correspond to different species or subspecies (Huchon *et al*., 1999; Gibb *et al*., 2016; Billet *et al*., 2017; Hautier *et al*., 2017; Feijó *et al*., 2018, 2019; Arteaga *et al*., 2020). Regarding allometry, our results show that the percentage of variation in skull shape due to the interaction between geography and size is weak at the ontogenetic level (R^2 = 3.16% - Fig. S4) and statistically unsupported at the static level. The slight difference in ontogenetic allometric trajectories among morphotypes of *D. novemcinctus* ssp. must be considered cautiously as it may be due to insufficient juvenile samplings in the Northern morphotype. A weak relationship between geography and allometry was also described in subspecies of the widespread Eurasian red squirrel (Marr & MacLeod, 2019), for which subtle and continuous mandibular shape changes were retrieved.

Our comparison of allometric patterns between the whole sample and the Southern morphotype in nine banded armadillos further demonstrates that overall cranial allometric patterns are well conserved within this potential species complex. While ecological factors such as diet can influence allometric patterns (Wilson, 2013), the distinction suggested by Smith & Redford (1990) between Central and South American populations (feeding more on termites and ants) and North American populations (more omnivorous) questions the influence of diet on allometric variation. But, the weak link between geography and allometry

549 in nine-banded armadillos also suggests that there is no clear influence of diet on overall
550 cranial allometric patterns either.
551
552 ## MAIN ALLOMETRIC VARIATIONS
553 ### *Entire Skull approach*
554 Allometry was recognized as an important component of mammalian skull variation, often
555 accounting for about a third of the cranial variation at intra- and interspecific levels in
556 mammals (Frost *et al*., 2003; Hallgrímsson *et al*., 2009; Cassini, 2013; Hallgrímsson *et al*.,
557 2015). Nine-banded armadillos are no exception with nearly 28% of the total cranial shape
558 variation explained by size at the ontogenetic level. The two major ontogenetic allometric
559 trends detected here were the relative snout elongation and the reduction of braincase
560 proportions, which is reminiscent of previous results dealing with mammalian species (Drake
561 & Klingenberg, 2008; Moyano *et al*., 2018; Heck *et al*., 2019). This pattern, often designated
562 as craniofacial allometry, was also detected at the evolutionary level in many groups of
563 mammals (Cardini & Polly, 2013; Cardini *et al*., 2015; Tamagnini *et al*., 2017). Cardini
564 (2019) proposed that craniofacial allometry could represent a much widespread pattern of
565 vertebrate morphological evolution.
566 In nine-banded armadillos, our analysis highlights some important additional
567 allometric patterns on the entire skull, which could be summarized as follows:
568 (i) The elongation of the snout is accompanied by a relative dorsoventral
569 flattening and a lateromedial narrowing. At the intraspecific level, previous
570 studies have also characterised a similar narrowing (e.g., Segura & Prevosti,
571 2012) or flattening (e.g., Ferreira-Cardoso *et al*., 2019) of the snout.
572 (ii) When size increases and the snout elongates, the length of the dental row
573 (excluding the M1; see Material and Methods) shortens relatively to the entire

skull at both the ontogenetic and static levels (Fig. 2), which might suggest that its size does not increase much during ontogeny. Several species belonging to the genus *Dasypus* stand out among extant armadillos in showing dental replacement of most of their cheek teeth (Ciancio *et al.*, 2011). Further research is needed to establish whether this allometric reduction of the dental row proportion is specific to nine-banded armadillos or more widespread in other xenarthran species. It is indeed worth noting that this variation is known to be reversed in other mammals such as pronghorns (Moyano *et al.*, 2020), zokors (Kang *et al.*, 2020) or howler monkeys (Meloro *et al.*, 2014) in which the relative length of the upper dental row increases relative to the length of the skull.

(iii) The orbitotemporal region shows a relative widening as the size increases, with a deeper post-orbital constriction, a dorsoventally higher zygomatic arch and a wider temporal fenestra. An allometric relationship between these two parts of the orbitotemporal region has already been described in a canid species (Segura & Prevosti, 2012) while in horses the opposite variation is observed (Heck *et al.*, 2019). It was noted that the effect of allometry throughout the orbitotemporal region is highly contrasted at the evolutionary level within mammalian groups, which is probably due to the functional relationship between the masticatory muscles and normal oculomotor function (Heesy, 2005).

(iv) Much of the allometric shape changes found at the static level were already detected with clearly higher proportions at the ontogenetic level, except for the parietal and palatine bones (Fig. 7A). The high proportion of static allometry for these two bones suggests that much of their size-related shape variation

599 occurs late during ontogeny (Fig. 6A), exhibits high phenotypic plasticity or is
600 subject to high selective pressure (Pélabon *et al*., 2013). This result is
601 particularly interesting in the case of long-nosed armadillos as their palatal
602 region bears several diagnostic traits for the genus *Dasypus* (Feijó & Cordeiro-
603 Estrela, 2016). It would be worth performing the same analyses in other
604 *Dasypus* species to see if this allometric pattern is conserved within
605 dasypodines and how it relates to the diagnostic features used to distinguish
606 species (Feijó *et al*., 2019).
607
608 *Bone-By-Bone (3B) approach and the complexity of cranial allometry*
609 Most studies on cranial allometry involved analyses of covariation between local cranial
610 distances and the skull length (e.g., Goswami & Prochel, 2007; Wilson, 2011; Wilson, 2013;
611 Wilson, 2018), or multivariate regressions over a set of cranial landmarks (GMM data) using
612 a whole-skull Procrustes alignment (e.g., Monteiro *et al*., 1999; Cardini & O'Higgins, 2005;
613 Heck *et al*., 2019; this study). A few studies, however, detailed allometric patterns on specific
614 regions of the skull with the use of linear distances (e.g., Billet *et al*., 2015). Our 3B analysis
615 may represent a novel approach, to our knowledge, as it uses geometric morphometrics to
616 pinpoint and compare allometric variations at a smaller anatomical scale, such as individual
617 bones, while changing the referential for the Procrustes alignment. Such an approach enabled
618 us to detect previously unnoticed allometric variations and to reveal an untapped complexity
619 of allometric patterns. The scrutiny of different spatial scales has important implications for
620 studies on morphological integration and modularity, because growth patterns and allometry
621 are essential factors for morphological integration (Porto *et al*., 2013; Klingenberg, 2013;
622 Mitteroecker *et al*., 2020). Such detailed characterisation of shape variation linked to size

623 should also help towards a better knowledge and more appropriate treatment of correlated
624 characters in morphological phylogenetics (Billet & Bardin, 2019).

625 The differences in allometric variation found in specific regions of the skull, with the
626 entire skull (ES) and 3B approaches at the ontogenetic and static levels, show that the whole
627 cranial allometric variation results from a complex superimposition of different allometric
628 patterns expressed at different times and locations. At the ontogenetic level, our 3B analyses
629 enabled to highlight major cranial allometric variations for most cranial units (OBUs; see
630 Material & Methods), which differ from the ones retrieved using the ES. For instance, a size-
631 related dorsoventral elongation and mediolateral shortening of the supraoccipital was detected
632 with the 3B approach but not with the ES analyses (Fig. 2, Fig. 5L1-L3). These results partly
633 agree with the bivariate analyses of Goswami & Prochel (2007), which showed that the width
634 of the supraoccipital followed an isometric growth in the common European mole (*Talpa*
635 *europaea* Linnaeus, 1758) while its height displayed positive allometry. Our 3B analyses also
636 highlighted that the processes of the nuchal crests undergo a strong posteromedial
637 development as size increases. Obviously, different allometric patterns could potentially be
638 detected when considering different scales (e.g., focus on the basicranium region instead of a
639 given bone).

640

641 HETEROGENEITY OF CRANIAL ALLOMETRY IN SPACE AND TIME

642 Our study shows that the degree of allometric shape variation is not homogeneously
643 distributed among the skull bones of nine-banded armadillos. Our 3B analyses most
644 particularly revealed that the allometric proportions of shape variation are regionalised.
645 Cranial units displaying the highest allometric proportions are not necessarily located close to
646 one another (Fig. 3). The relation with cranial size differs between OBUs, which is in line
647 with bivariate analyses demonstrating that most distances measured on mammalian skulls

follow different allometric trends (e.g., Abdala *et al*., 2001; Marroig & Cheverud, 2004; Goswami & Prochel, 2007; Wilson, 2011; Segura & Prevosti, 2012; Moyano *et al*., 2018). This heterogeneity of allometric proportions per cranial unit could not be explained by the variation in size during ontogeny (see Results and Figs. 6A-B, 7A). Similarly, both the prenatal skull ossification sequence (Fig. 7C – see Hautier *et al*., 2011) and the embryonic origin of each bone (Fig. 7D – see Piekarski *et al*., 2014) could not explain the differences in allometric proportions observed. Slight methodological artefacts (e.g., number of landmarks per object) and the multiplicity of developmental and genetic processes at stake during local cranial morphogenesis (Hallgrímsson *et al*., 2019) may explain the heterogeneous pattern found in our study. In addition, the proportion of total shape variation of each cranial unit explained by an independent variable, here size, may also depend on how much other variables (e.g., environment) explain total shape variation and how these overlap with size.

We demonstrated that cranial units located in the anterior half of the skull vary more in size during postnatal development than those in the posterior half (Figs. 6B, 7A – see Segura & Prevosti, 2012 for another example in Canidae). This result echoes the ontogenetic pattern of allometric variation of the entire skull where a clear separation could be made between the snout and braincase (Fig. 2). In contrast to the mosaic distribution of allometric proportions, such a division of the skull into two parts (or modules) is more congruent with the skull ossification sequence and the embryonic origin of each bone (with the exclusion of the squamosal) (Fig. 7).

Considering several ontogenetic stages contribute to a better understanding of the relative influences of the various developmental periods to the observed allometric patterns (Klingenberg & Zimmermann, 1992; Mitteroecker *et al*., 2013). Although preliminary, and pending confirmation for each morphotype, our results show that the allometric proportion of shape variation regularly decreases with age for the entire skull, as well as for most cranial

673 units (Fig. 6A), as could be expected for mammals (finite growth). However, the allometric
674 proportions over time differ between cranial units as illustrated by OBUs having higher
675 allometric proportions at the juvenile stage than at other stages (maxillary, frontal, bo-eo OBU
676 and petrosal), and OBUs displaying higher or better supported allometric proportions in
677 subadults and adults than in juveniles (palatine and parietal) (Fig. 6A). We thus characterized
678 a partition across developmental stages in each cranial unit, superimposed to the partition in
679 the allometric proportion of shape variation among cranial bones. This heterogeneity of
680 cranial allometry in time and space in nine-banded armadillos strongly suggests the existence
681 of a complex modular architecture. Such modularity might facilitate the evolvability of the
682 phenotype and be a prerequisite for heterochronic evolutionary changes, which are often local
683 and mosaic (Mitteroecker *et al*., 2004; Gerber & Hopkins, 2011).

684 Several authors (Zumpano & Richtsmeier 2003; Goswami & Prochel, 2007; Sardi *et*
685 *al*., 2007; Wilson, 2011) have shown that birth may constitute a clear-cut transition in the
686 growth dynamics of several cranial units in rodents and primates, especially for the cranial
687 roof. Since nine-banded armadillos are precocial (Derrickson, 1992; Krmpotic *et al*., 2012),
688 much of the allometric variation patterns found in our postnatal sample may also be expressed
689 prenatally (Zelditch *et al*., 2003; Wilson; 2018), a hypothesis that could be tested on a sample
690 including foetuses. These analyses of allometric patterns could also be performed in different
691 armadillo species, at both the intraspecific and interspecific levels, to see how allometric
692 patterns are comparable between species and whether they are maintained at an evolutionary
693 scale (e.g., Gerber *et al*., 2008; Esquerré *et al*., 2017; Wilson, 2018).
694
695 **ACKNOWLEDGMENTS**
696

We are grateful to Christiane Denys, Violaine Nicolas, and Géraldine Véron, (*Muséum National d'Histoire Naturelle*, Paris, France), Roberto Portela Miguez, Louise Tomsett, and Laura Balcells (British Museum of Natural History, London, UK), Eileen Westwig (American Museum of Natural History, New York, USA), Nicole Edmison and Chris Helgen (National Museum of Natural History, Washington, DC, USA), Jake Esselstyn (Louisiana State University, Museum of Natural Sciences, Baton Rouge, USA), Manuel Ruedi (*Muséum d'Histoire Naturelle*, Geneva, Switzerland) for access to comparative material. We thank Benoit de Thoisy (*Institut Pasteur de la Guyane*) and Clara Belfiore for their help with the data acquisition, Cyril Le Verger for his help in the 3D isolation of cranial units, Rémi Lefebvre (*Muséum National d'Histoire Naturelle*) for his help on the definition of internal landmarks, Sérgio Ferreira-Cardoso (*Institut des Sciences de l'Evolution*) and Olivia Plateau (University of Fribourg, Switzerland) for interesting discussions on covariation patterns, and Christian de Muizon (*Muséum National d'Histoire Naturelle*) for anatomical discussions. Renaud Lebrun (*Institut des Sciences de l'Evolution*), Farah Ahmed (British Museum of Natural History), Miguel García-Sanz and Florent Goussard (Platform AST-RX – *Muséum National d'Histoire Naturelle*) generously provided help and advice on the acquisition of CT scans. Finally, we thank Nilton Cáceres (Federal University of Santa Maria, Brazil) and an anonymous reviewer, for their helpful comments. Some of the experiments were performed using the µ-CT facilities of the Montpellier Rio Imaging (MRI) platform of the LabEx CeMEB. This work has benefited from an "Investissements d'Avenir" grant managed by *Agence Nationale de la Recherche*, France (CEBA, ref. ANR-10-LABX-25-01). This research received support from the Synthesys Project (http://synthesys3.myspecies.info/), which is funded by the European Community Research Infrastructure Action under the FP7. This is contribution ISEM 2020-XXX of the *Institut des Sciences de l'Evolution de Montpellier*.

REFERENCES

Abba AM, Cassini GH, Valverde G, Tilak MK, Vizcaíno SF, Superina M, Delsuc F. 2015. Systematics of hairy armadillos and the taxonomic status of the Andean hairy armadillo (*Chaetophractus nationi*). *Journal of Mammalogy* 96: 673–689.

Abdala F, Flores DA, Giannini NP. 2001. Postweaning ontogeny of the skull of *Didelphis albiventris*. *Journal of Mammalogy* 82: 190–200.

Adams DC, Rohlf FJ, Slice DE. 2013. A field comes of age: geometric morphometrics in the 21st century. *Hystrix, the Italian Journal of Mammalogy* 24: 7–14.

Adams DC, Collyer ML, Kaliontzopoulou A. 2018. Geomorph: Software for geometric morphometric analyses. R package version 3.0.7. R Foundation for Statistical Computing, Vienna, Austria.

Adams DC, Collyer ML, Kaliontzopoulou A. 2019. Geomorph: Software for geometric morphometric analyses. R package version 3.1.1. R Foundation for Statistical Computing, Vienna, Austria.

Anderson MJ. 2001. A new method for non-parametric multivariate analysis of variance. *Austral ecology* 26: 32–46.

Arteaga MC, Gasca-Pineda J, Bello-Bedoy R, Eguiarte LE, Medellin RA. 2020. Conservation Genetics, Demographic History, and Climatic Distribution of the Nine-Banded Armadillo

(*Dasypus novemcinctus*): An Analysis of Its Mitochondrial Lineages. In: Ortega J, Maldonado JE, eds. *Conservation Genetics in Mammals: Integrative Research Using Novel Approaches*. Switzerland: Springer-Cham, 141–163.

Baker J, Meade A, Pagel M, Venditti C. 2015. Adaptive evolution toward larger size in mammals. *Proceedings of the National Academy of Sciences* 112: 5093–5098.

Billet G, Hautier L, De Muizon C, Valentin X. 2011. Oldest cingulate skulls provide congruence between morphological and molecular scenarios of armadillo evolution. *Proceedings of the Royal Society B: Biological Sciences* 278: 2791–2797.

Billet G, De Muizon C, Schellhorn R, Ruf I, Ladevèze S, Bergqvist L. 2015. Petrosal and inner ear anatomy and allometry amongst specimens referred to Litopterna (Placentalia). *Zoological Journal of the Linnean Society* 173: 956–987.

Billet G, Hautier L, De Thoisy B, Delsuc F. 2017. The hidden anatomy of paranasal sinuses reveals biogeographically distinct morphotypes in the nine-banded armadillo (*Dasypus novemcinctus*). *PeerJ* 5: e3593.

Billet G, Bardin J. 2019. Serial Homology and Correlated Characters in Morphological Phylogenetics: Modeling the Evolution of Dental Crests in Placentals. *Systematic Biology* 68: 267–280.

770 Bokma F, Godinot M, Maridet O, Ladevèze S, Costeur L, Solé F, Gheerbrant E, Peigné S,
771 Jacques F, Laurin M. 2016. Testing for Depéret's rule (body size increase) in mammals using
772 combined extinct and extant data. *Systematic biology* 65: 98–108.
773
774 Bubadué JM, Cáceres N, Carvalho RS, Meloro C. 2015. Ecogeographical variation in skull
775 shape of South-American canids: abiotic or biotic processes? *Evolutionary Biology* 43:
776 145e159.
777
778 Cardini A. 2019. Craniofacial allometry is a rule in evolutionary radiations of placentals.
779 *Evolutionary Biology* 46: 239–248.
780
781 Cardini A, O'Higgins P. 2005. Post-natal ontogeny of the mandible and ventral cranium in
782 *Marmota* species (Rodentia, Sciuridae): allometry and phylogeny. *Zoomorphology* 124: 189–
783 203.
784
785 Cardini A, Polly PD. 2013. Larger mammals have longer faces because of size-related
786 constraints on skull form. *Nature communications* 4: 2458.
787
788 Cardini A, Polly D, Dawson R, Milne N. 2015. Why the long face? Kangaroos and wallabies
789 follow the same 'rule' of cranial evolutionary allometry (CREA) as placentals. *Evolutionary*
790 *Biology* 42: 169–176.
791
792 Cassini GH. 2013. Skull geometric morphometrics and paleoecology of Santacrucian (Late
793 Early Miocene; Patagonia) native ungulates (Astrapotheria, Litopterna, and Notoungulata).
794 *Ameghiniana* 50: 193–216.

795

796 Ciancio MR, Castro MC, Galliari FC, Carlini AA, Asher RJ. 2011. Evolutionary implications
797 of dental eruption in *Dasypus* (Xenarthra). *Journal of Mammalian Evolution* 19: 1–8.
798

799 Costa FR, Clerici GP, Lobo-Ribeiro L, Rosa PS, Rocha-Barbosa O. 2019. Analysis of the
800 spatio-temporal parameters of gaits in *Dasypus novemcinctus* (Xenarthra: Dasypodidae). *Acta*
801 *Zoologica* 100: 61–68.
802

803 Collyer ML, Adams DC. 2013. Phenotypic trajectory analysis: comparison of shape change
804 patterns in evolution and ecology. *Hystrix, the Italian Journal of Mammalogy* 24: 75.
805

806 Collyer ML, Sekora DJ, Adams DC. 2015. A method for analysis of phenotypic change for
807 phenotypes described by high-dimensional data. *Heredity* 115: 357.
808

809 Delsuc F, Gibb GC, Kuch M, Billet G, Hautier L, Southon J, Rouillard JM, Fernicola JC,
810 Vizcaíno SF, MacPhee RDE, Poinar HN. 2016. The phylogenetic affinities of the extinct
811 glyptodonts. *Current Biology* 26: R155–R156.
812

813 Derrickson EM. 1992. Comparative reproductive strategies of altricial and precocial eutherian
814 mammals. *Functional Ecology*: 57–65.
815

816 Drake AG, Klingenberg CP. 2008. The pace of morphological change: historical
817 transformation of skull shape in St Bernard dogs. *Proceedings of the Royal Society B:*
818 *Biological Sciences* 275: 71–76.
819

820 Dushoff J, Kain MP, Bolker BM. 2019. I can see clearly now: reinterpreting statistical
821 significance. *Methods in Ecology and Evolution* 10: 756–759.
822
823 Esquerré D, Sherratt E, Keogh JS. 2017. Evolution of extreme ontogenetic allometric
824 diversity and heterochrony in pythons, a clade of giant and dwarf snakes. *Evolution* 71: 2829–
825 2844.
826
827 Feijó A, Cordeiro-Estrela P. 2016. Taxonomic revision of the *Dasypus kappleri* complex,
828 with revalidations of *Dasypus pastasae* (Thomas, 1901) and *Dasypus beniensis* Lönnberg,
829 1942 (Cingulata, Dasypodidae). *Zootaxa* 4170: 271–297.
830
831 Feijó A, Patterson BD, Cordeiro-Estrela P. 2018. Taxonomic revision of the long-nosed
832 armadillos, Genus *Dasypus* Linnaeus, 1758 (Mammalia, Cingulata). *PloS one* 13: e0195084.
833
834 Feijó A, Vilela JF, Cheng J, Schetino MAA, Coimbra RTF, Bonvicino CR, Santos FR,
835 Patterson BD, Cordeiro-Estrela P. 2019. Phylogeny and molecular species delimitation of
836 long-nosed armadillos (*Dasypus*: Cingulata) supports morphology-based taxonomy.
837 *Zoological Journal of the Linnean Society* 186: 813–825.
838
839 Ferreira-Cardoso S, Billet G, Gaubert P, Delsuc F, Hautier L. 2019. Skull shape variation in
840 extant pangolins (Pholidota: Manidae): allometric patterns and systematic implications.
841 *Zoological Journal of the Linnean Society* 188: 255–275.
842
843 Frappell PB, Boggs DF, Kilgore Jr DL. 1998. How stiff is the armadillo?: A comparison with
844 the allometrics of mammalian respiratory mechanics. *Respiration physiology* 113: 111–122.

Frost SR, Marcus LF, Bookstein FL, Reddy DP, Delson E. 2003. Cranial allometry, phylogeography, and systematics of large-bodied papionins (primates: Cercopithecinae) inferred from geometric morphometric analysis of landmark data. *The Anatomical Record Part A: Discoveries in Molecular, Cellular, and Evolutionary Biology: An Official Publication of the American Association of Anatomists* 275: 1048–1072.

Gaudin T, Wible JR. 2006. The phylogeny of living and extinct armadillos (Mammalia, Xenarthra, Cingulata): a craniodental analysis. In: Carrano MT, Gaudin TJ, Blob RW, Wible JR, eds. *Amniote Paleobiology: Perspectives on the Evolution of Mammals, Birds, and Reptiles*. Chicago: University of Chicago Press, 153–198.

Gerber S, Eble GJ, Neige P. 2008. Allometric space and allometric disparity: a developmental perspective in the macroevolutionary analysis of morphological disparity. *Evolution: International Journal of Organic Evolution* 62: 1450–1457.

Gerber S, Hopkins MJ. 2011. Mosaic heterochrony and evolutionary modularity: the trilobite genus *Zacanthopsis* as a case study. *Evolution: International Journal of Organic Evolution* 65: 3241–3252.

Gibb GC, Condamine FL, Kuch M, Enk J, Moraes-Barros N, Superina M, Poinar HN, Delsuc F. 2016. Shotgun mitogenomics provides a reference phylogenetic framework and timescale for living xenarthrans. *Molecular Biology and Evolution* 33: 621–642.

869 Good PI. 2000. *Permutation tests: a practical guide to resampling methods for testing*
870 *hypotheses*. Berlin: Springer-Verlag, 2nd eds.
871
872 Goodall C. 1991. Procrustes methods in the statistical analysis of shape. *Journal of the Royal*
873 *Statistical Society: Series B (Methodological)* 53: 285–321.
874
875 Goswami A, Prochel J. 2007. Ontogenetic morphology and allometry of the cranium in the
876 common European mole (*Talpa europaea*). *Journal of Mammalogy* 88: 667–677.
877
878 Goswami A, Finarelli JA. 2016. EMMLi: a maximum likelihood approach to the analysis of
879 modularity. *Evolution* 70: 1622–1637.
880
881 Hallgrímsson B, Jamniczky H, Young NM, Rolian C, Parsons TE, Boughner JC, Marcucio
882 RS. 2009. Deciphering the palimpsest: studying the relationship between morphological
883 integration and phenotypic covariation. *Evolutionary biology* 36: 355–376.
884
885 Hallgrímsson B, Percival CJ, Green R, Young NM, Mio W, Marcucio R. 2015.
886 Morphometrics, 3D imaging, and craniofacial development. *In Current topics in*
887 *developmental biology* 115: 561–597.
888
889 Hallgrímsson B, Katz DC, Aponte JD, Larson JR, Devine J, Gonzalez PN, Young NM,
890 Roseman CC, Marcucio RS. 2019. Integration and the Developmental Genetics of Allometry.
891 *Integrative and comparative biology* 59: 1369–1381.
892

Hautier L, Weisbecker V, Goswami A, Knight F, Kardjilov N, Asher RJ. 2011. Skeletal ossification and sequence heterochrony in xenarthran evolution. *Evolution & development* 13: 460–476.

Hautier L, Billet G, De Thoisy B, Delsuc F. 2017. Beyond the carapace: skull shape variation and morphological systematics of long-nosed armadillos (genus *Dasypus*). *PeerJ* 5: e3650.

Heck L, Sánchez-Villagra MR, Stange M. 2019. Why the long face? Comparative shape analysis of miniature, pony, and other horse skulls reveals changes in ontogenetic growth. *PeerJ* 7: e7678.

Heesy CP. 2005. Function of the mammalian postorbital bar. *Journal of Morphology* 264: 363–380.

Hoffman EA, Rowe TB. 2018. Jurassic stem-mammal perinates and the origin of mammalian reproduction and growth. *Nature* 561: 104.

Huchon D, Delsuc F, Catzeflis FM, Douzery EJ. 1999. Armadillos exhibit less genetic polymorphism in North America than in South America: nuclear and mitochondrial data confirm a founder effect in *Dasypus novemcinctus* (Xenarthra). *Molecular Ecology* 8: 1743–1748.

Izenman AJ. 2013. Multivariate regression. In: Izenman AJ, ed. *Modern Multivariate Statistical Techniques*. New York: Springer-Verlag, 159–194.

Kang Y, Su J, Yao B, Ji W, Hegab IM, Hanafy AM, Zhang D. 2020. Geometric morphometric analysis of the plateau zokor (*Eospalax baileyi*) revealed significant effects of environmental factors on skull variations. *Zoology*: 125779.

Klingenberg CP. 2013. Cranial integration and modularity: insights into evolution and development from morphometric data. *Hystrix, the Italian Journal of Mammalogy* 24: 43–58.

Klingenberg CP. 2016. Size, shape, and form: concepts of allometry in geometric morphometrics. *Development genes and evolution* 226: 113–137.

Klingenberg CP, Zimmermann M. 1992. Static, ontogenetic, and evolutionary allometry: a multivariate comparison in nine species of water striders. *The American Naturalist* 140: 601–620.

Klingenberg CP, McIntyre GS. 1998. Geometric morphometrics of developmental instability: analyzing patterns of fluctuating asymmetry with Procrustes methods. *Evolution* 52: 1363–1375.

Klingenberg CP, Barluenga M, Meyer A. 2002. Shape analysis of symmetric structures: quantifying variation among individuals and asymmetry. *Evolution* 56: 1909–1920.

Krmpotic CM, Galliari FC, Barbeito CG, Carlini AA. 2012. Development of the integument of *Dasypus hybridus* and *Chaetophractus vellerosus*, and asynchronous events with respect to the postcranium. *Mammalian Biology - Zeitschrift für Säugetierkunde* 77: 314–326.

943 Linde-Medina M. 2016. Testing the cranial evolutionary allometric ‘rule’ in Galliformes.
944 *Journal of evolutionary biology* 29: 1873–1878.
945
946 Linnaeus C. 1758. *Systema naturae per regna tria naturæ, secundum classes, ordines, genera,*
947 *species, cum characteribus, differentiis, synonymis, locis. Tomus I. Editio decima, reformata*.
948 Homiae: Laurentii Salvii.
949
950 Marr MM, MacLeod N. 2019. Geographical variation in Eurasian red squirrel (*Sciurus*
951 *vulgaris* L., 1758) mandibles and the issue of subspecies-level organization: a failure of
952 history? *Biological Journal of the Linnean Society* 128: 337–359.
953
954 Marroig G, Cheverud JM. 2004. Cranial evolution in sakis (Pithecia, Platyrrhini) I:
955 interspecific differentiation and allometric patterns. *American Journal of Physical*
956 *Anthropology: The Official Publication of the American Association of Physical*
957 *Anthropologists* 125: 266–278.
958
959 Meloro C, Cáceres N, Carotenuto F, Passaro F, Sponchiado J, Melo GL, Raia P. 2014.
960 Ecogeographical variation in skull morphometry of howler monkeys (Primates: Atelidae).
961 *Zoologischer Anzeiger* 253: 345e359.
962
963 Mitteroecker P, Gunz P, Weber GW, Bookstein FL. 2004. Regional dissociated heterochrony
964 in multivariate analysis. *Annals of Anatomy - Anatomischer Anzeiger* 186: 463–470.
965

966 Mitteroecker P, Gunz, P, Windhager S, Schaefer K. 2013. A brief review of shape, form, and
967 allometry in geometric morphometrics, with applications to human facial morphology.
968 *Hystrix* 24: 59–66.
969
970 Mitteroecker P, Bartsch S, Erkinger C, Grunstra NDS, Le Maître A, Bookstein FL. 2020.
971 Morphometric Variation at Different Spatial Scales: Coordination and Compensation in the
972 Emergence of Organismal Form. *Systematic Biology*: syaa007
973
974 Moeller W. 1968. Allometrische analyse der gürteltierschädel. Ein beitrag zur phylogenie der
975 Dasypodidae Bonaparte, 1838. *Zoologische Jahrbücher. Abteilung für Anatomie und*
976 *Ontogenie der Tiere* 85: 411–528.
977
978 Monteiro LR, Less LG, Abe AS. 1999. Ontogenetic variation in skull shape of *Thrichomys*
979 *apereoides* (Rodentia: Echimyidae). *Journal of Mammalogy* 80: 102–111.
980
981 Moyano SR, Cassini GH, Giannini NP. 2018. Skull Ontogeny of the Hyraxes *Procavia*
982 *capensis* and *Dendrohyrax arboreus* (Procaviidae: Hyracoidea). *Journal of Mammalian*
983 *Evolution* 26: 317–331.
984
985 Moyano SR, Morales MM, Giannini NP. 2020. Skull ontogeny of the pronghorn (*Antilocapra*
986 *americana*) in the comparative context of native North American ungulates. *Canadian*
987 *Journal of Zoology* 98: 165–174.
988
989 Nummela S. 1995. Scaling of the mammalian middle ear. *Hearing research* 85: 18–30.
990

991 Pélabon C, Bolstad GH, Egset CK, Cheverud JM, Pavlicev M, Rosenqvist G. 2013. On the
992 relationship between ontogenetic and static allometry. *The American Naturalist* 181: 195–
993 212.
994
995 Piekarski N, Gross JB, Hanken J. 2014. Evolutionary innovation and conservation in the
996 embryonic derivation of the vertebrate skul. *Nature Communications* 5: 5661.
997
998 Porto A, Shirai LT, de Oliveira FB, Marroig G. 2013. Size variation, growth strategies, and
999 the evolution of modularity in the mammalian skull. *Evolution* 67: 3305–3322.
1000
1001 Price SA, Hopkins SS. 2015. The macroevolutionary relationship between diet and body mass
1002 across mammals. *Biological Journal of the Linnean Society* 115: 173–184.
1003
1004 Rohlf FJ, Slice D. 1990. Extensions of the Procrustes method for the optimal superimposition
1005 of landmarks. *Systematic Biology* 39: 40–59.
1006
1007 Ross CF, Metzger KA. 2004. Bone strain gradients and optimization in vertebrate skulls.
1008 *Annals of Anatomy-Anatomischer Anzeiger* 186: 387–396.
1009
1010 Sánchez-Villagra MR. 2012. *Embryos in deep time: the rock record of biological*
1011 *development*. San Francisco: University of California Press.
1012
1013 Sardi ML, Ventrice F, Rozzi FR. 2007. Allometries throughout the late prenatal and early
1014 postnatal human craniofacial ontogeny. *The Anatomical Record: Advances in Integrative*
1015 *Anatomy and Evolutionary Biology* 290: 1112–1120.

1016

1017 Schlager S. 2017. Morpho and Rvcg – Shape Analysis in R: R-Packages for Geometric
1018 Morphometrics, Shape Analysis and Surface Manipulations. In: Zheng G, Li S, Szekely G,
1019 eds. *Statistical Shape and Deformation Analysis*. London: Academic Press, 217–256.

1020

1021 Schneider CA, Rasband WS, Eliceiri KW. 2012. NIH Image to ImageJ: 25 years of image
1022 analysis. *Nature methods* 9: 671.

1023

1024 Segura V, Prevosti F. 2012. A quantitative approach to the cranial ontogeny of *Lycalopex*
1025 *culpaeus* (Carnivora: Canidae). *Zoomorphology* 131: 79–92.

1026

1027 Sibly RM, Brown JH. 2007. Effects of body size and lifestyle on evolution of mammal life
1028 histories. *Proceedings of the National Academy of Sciences* 104: 17707–17712.

1029

1030 Slater GJ, Van Valkenburgh B. 2009. Allometry and performance: the evolution of skull form
1031 and function in felids. *Journal of evolutionary biology* 22: 2278–2287.

1032

1033 Slijper EJ. 1962. *Whales*. London: Hutchinson and Co.

1034

1035 Smith K, Redford KH. 1990. The anatomy and function of the feeding apparatus in two
1036 armadillos (Dasypoda): anatomy is not destiny. *Journal of Zoology* 222: 27–47.

1037

1038 Smith FA, Boyer AG, Brown JH, Costa DP, Dayan T, Ernest SKM, Evans AR, Fortelius M,
1039 Gittleman JL, Hamilton MJ, Harding LE, Lintulaakso K, Lyons SK, McCain C, Okie1 JG,

1040 Saarinen JJ, Sibly RM, Stephens PR, Theodor J, Uhen MD. 2010. The evolution of maximum
1041 body size of terrestrial mammals. *Science* 330: 1216–1219.
1042
1043 Superina M, Abba AM. 2018. Family Chlamyphoridae (Chlamyphorid armadillos).
1044 *Handbook of the mammals of the world* 8: 48–73.
1045
1046 Tamagnini D, Meloro C, Cardini A. 2017. Anyone with a long-face? Craniofacial
1047 Evolutionary Allometry (CREA) in a family of short-faced mammals, the Felidae.
1048 *Evolutionary Biology* 44: 476–495.
1049
1050 Vizcaíno SF, Milne N. 2002. Structure and function in armadillo limbs (Mammalia:
1051 Xenarthra: Dasypodidae). *Journal of Zoology* 257: 117–127.
1052
1053 Vizcaíno SF, Cassini GH, Toledo N, Bargo MS. 2012. On the evolution of large size in
1054 mammalian herbivores of Cenozoic. In: Patterson BP, Costa LP, eds. *Bones, Clones and*
1055 *Biomes: an 80-million year History of Recent Neotropical Mammals*. Chicago and London:
1056 The University of Chicago Press, 76-101.
1057
1058 Wetzel RM, Mondolfi E. 1979. The subgenera and species of long-nosed armadillos, genus
1059 *Dasypus* L. In: Eisenberg JF, ed. *Vertebrate ecology in the northern Neotropics*. Washington:
1060 Smithsonian Institution Press, 43-63.
1061
1062 Wilson LA. 2011. Comparison of prenatal and postnatal ontogeny: cranial allometry in the
1063 African striped mouse (*Rhabdomys pumilio*). *Journal of Mammalogy* 92: 407–420.
1064

Wilson LA. 2013. Allometric disparity in rodent evolution. *Ecology and evolution* 3: 971–984.

Wilson LA. 2018. The evolution of ontogenetic allometric trajectories in mammalian domestication. *Evolution* 72: 867–877.

Zelditch ML, Sheets HD, Fink WL. 2003. The ontogenetic dynamics of shape disparity. *Paleobiology* 29: 139–156.

Zumpano MP, Richtsmeier JT. 2003. Growth-related shape changes in the fetal craniofacial complex of humans (*Homo sapiens*) and pigtailed macaques (*Macaca nemestrina*): a 3D-CT comparative analysis. *American Journal of Physical Anthropology* 120: 339–351.

FIGURE CAPTIONS

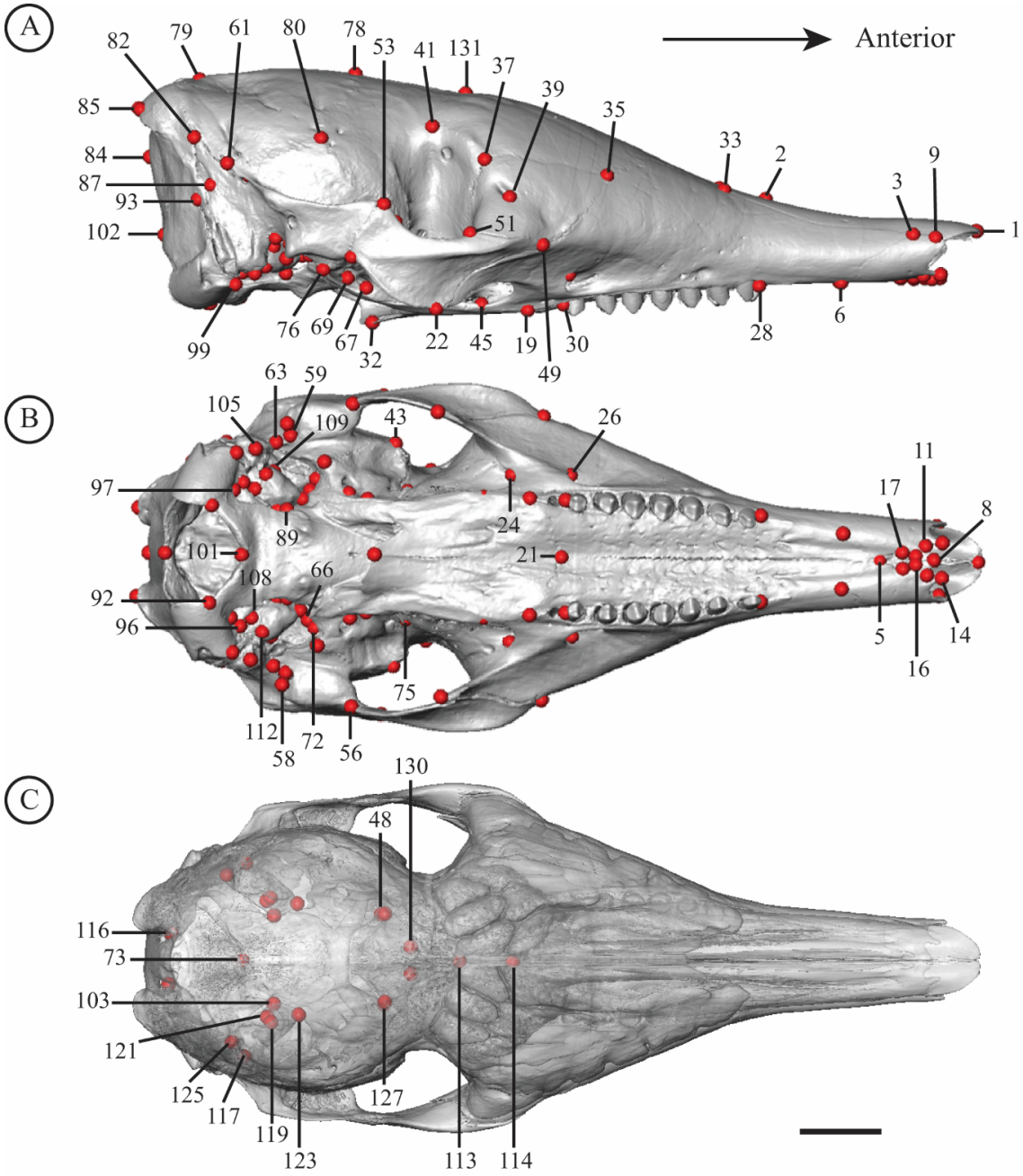

Figure 1. Landmarks digitized on the skull of *Dasypus novemcinctus* (MNHN.CG.2006-565). Lateral (A), ventral (B), and dorsal (C) views. The skull in dorsal view is shown with bone transparency (25%). Scale-bar = 1 cm. List of landmarks can be found in Table 1 and Table 2.

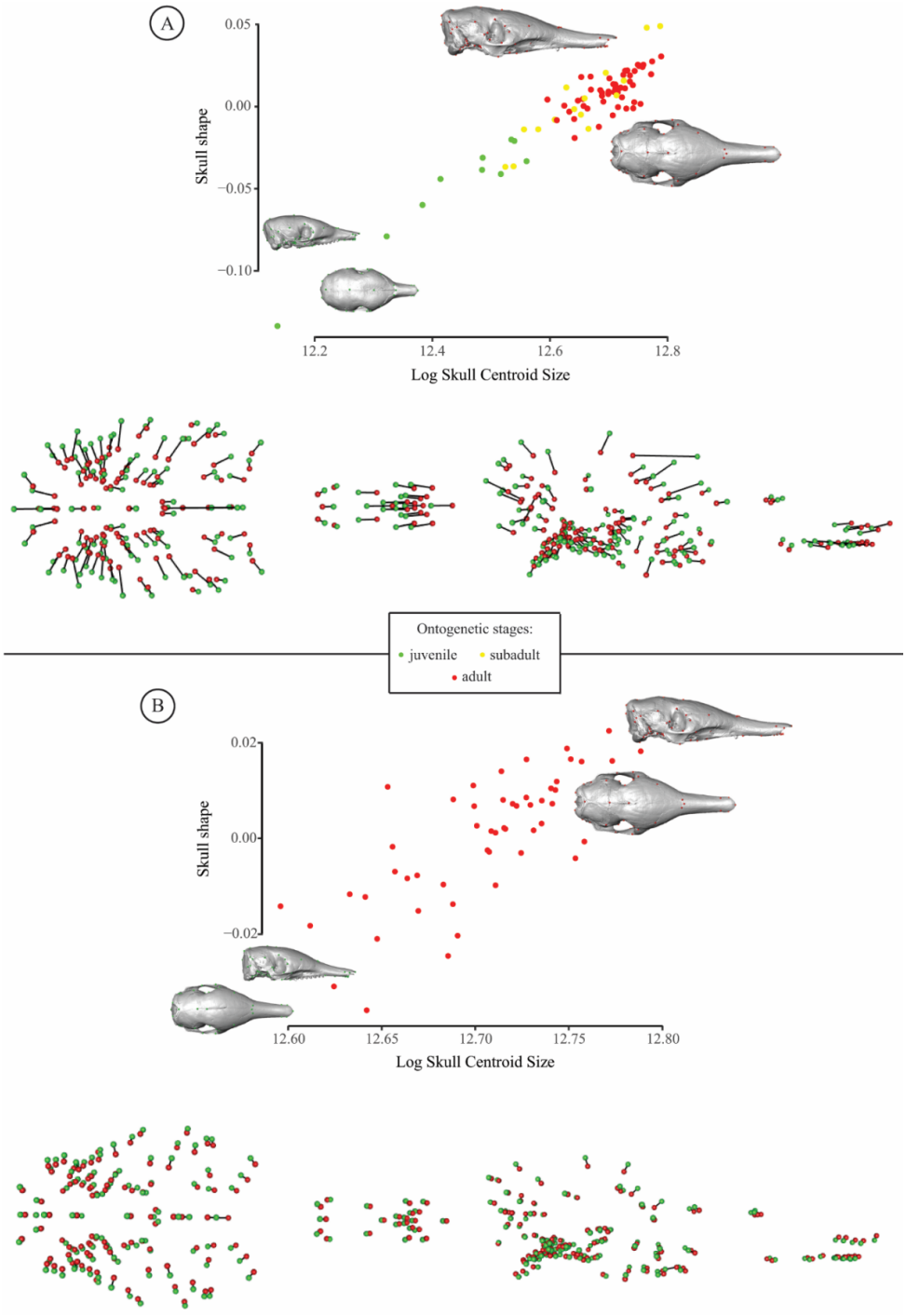

Figure 2. Ontogenetic and static allometry on the entire skull (ES) of nine-banded armadillos. Ontogenetic stages are represented with different colours (juvenile = green; subadult = yellow; adult = red; see text for more detail). For graphical display, we used the projected regression scores of the shape data to represent shape variation related to changes in log centroid size (Adams *et al*., 2013). Shape changes were visualized as vectors from the minimal shape (green) to the maximal shape (red) of the shape regression scores corresponding to the projection of the data points in shape space on to an axis in the direction of the regression vector (see Drake & Klingenberg, 2008). A. Multivariate regression of skull shape on log skull centroid size at the ontogenetic level, representing 27.62% of the total shape variation. B. Same analysis, at the static level (6.31% of total shape variation) (see text).

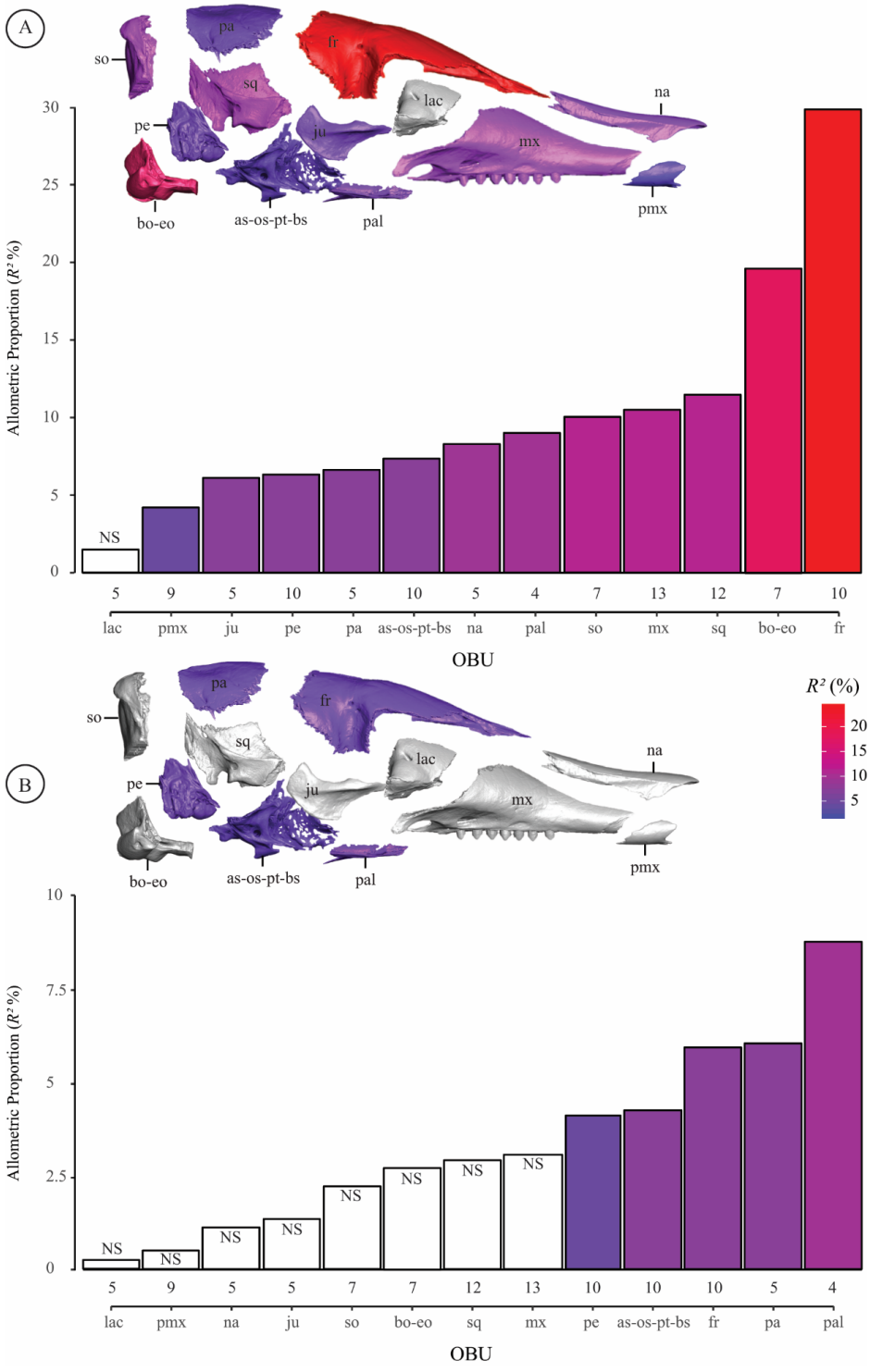

Figure 3. Bar graphs showing the allometric proportions (R^2) of each cranial unit's (OBU) total shape variation under the 3B approach (see text), at the ontogenetic (A) and static (B) levels. Allometric proportions are shown with the log skull centroid size taken as size variable. On the virtually dislocated skull (in right lateral view), the allometric proportions are reported in corresponding colours. White bars indicate a statistically unsupported (NS) allometry for a given OBU (at *p value* > 0.05). Abbreviations of OBUs: as-os-pt-bs, alisphenoid-orbitosphenoid-pterygoid-basisphenoid complex; bo-eo, basioccipital-exoccipital complex; fr, frontal; ju, jugal; lac, lacrimal; mx, maxillary; na, nasal; pa, parietal; pal, palatine; pe, petrosal; pmx, premaxillary; so, supraoccipital; sq, squamosal.

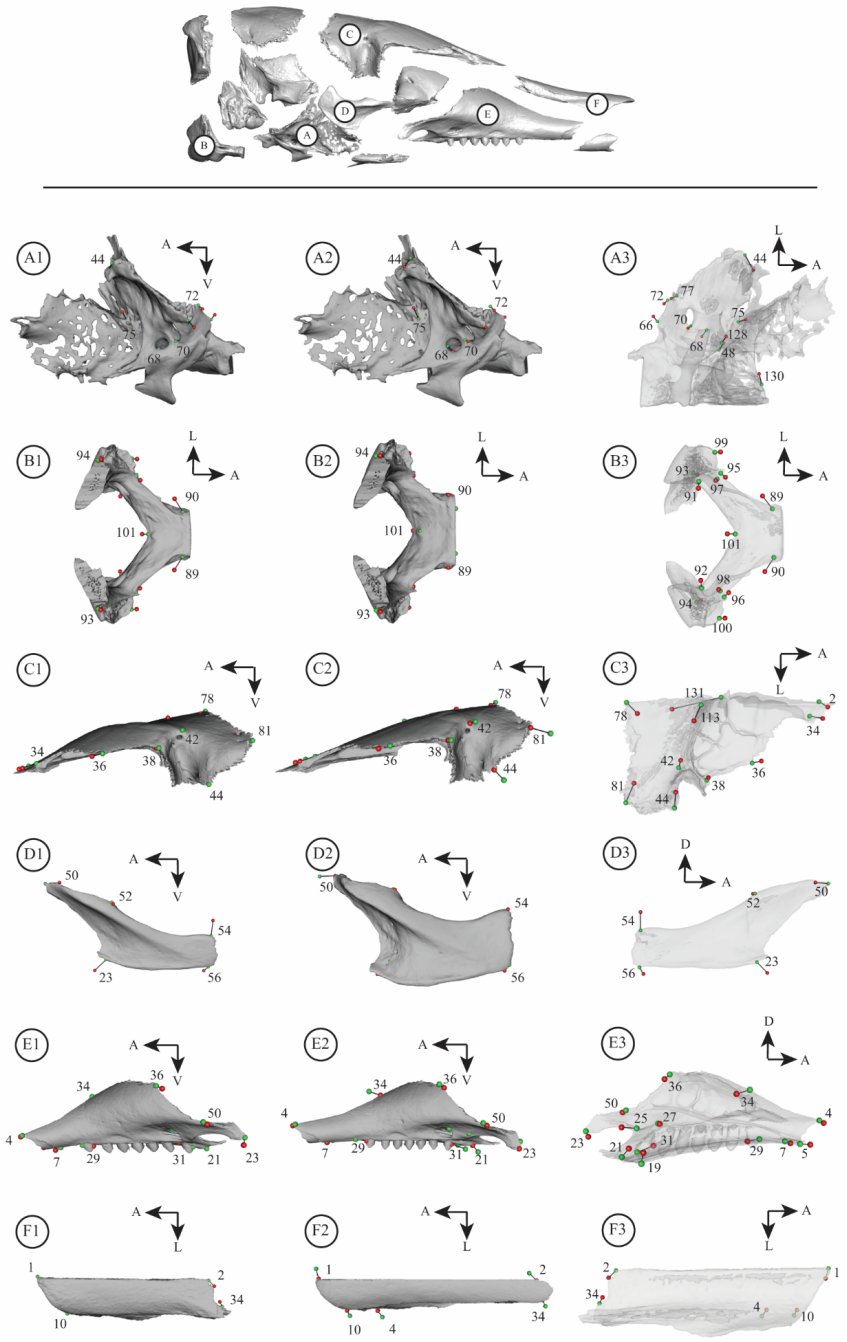

Figure 4. Vector representation of the allometric shape changes detected for a given cranial unit (OBU), represented between its minimal (green – smaller centroid size) and maximal (red – larger centroid size) shape (see Fig. 2). Results of the analysis performed at the ontogenetic level, and with the log skull centroid size taken as the size variable (see text). For each OBU, the changes are shown in three subsections organized horizontally: 1, vectors from minimal to maximal shape with minimal OBU shape; 2, same as 1) with maximal OBU shape; 3, minimal OBU shape in transparency with vectors. A) alisphenoid-orbitosphenoid-pterygoid-basisphenoid complex; A1-A2, lateral view; A3, dorsal view. B) basioccipital-exoccipital complex; B1-B2, dorsal view; B3, ventral view. C) frontal; C1-C2, lateral view; C3, ventral view. D) jugal; D1-D2, lateral view; D3, medial view. E) maxillary; E1-E2, lateral view; E3, medial view. F) nasal; F1-2, dorsal view; F3, ventral view. Landmark numbers and orientation arrows were added for more readability as well as the overall representation of the unpaired bone (basioccipital). Abbreviations: A, anterior; D, dorsal; L, lateral; V, ventral.

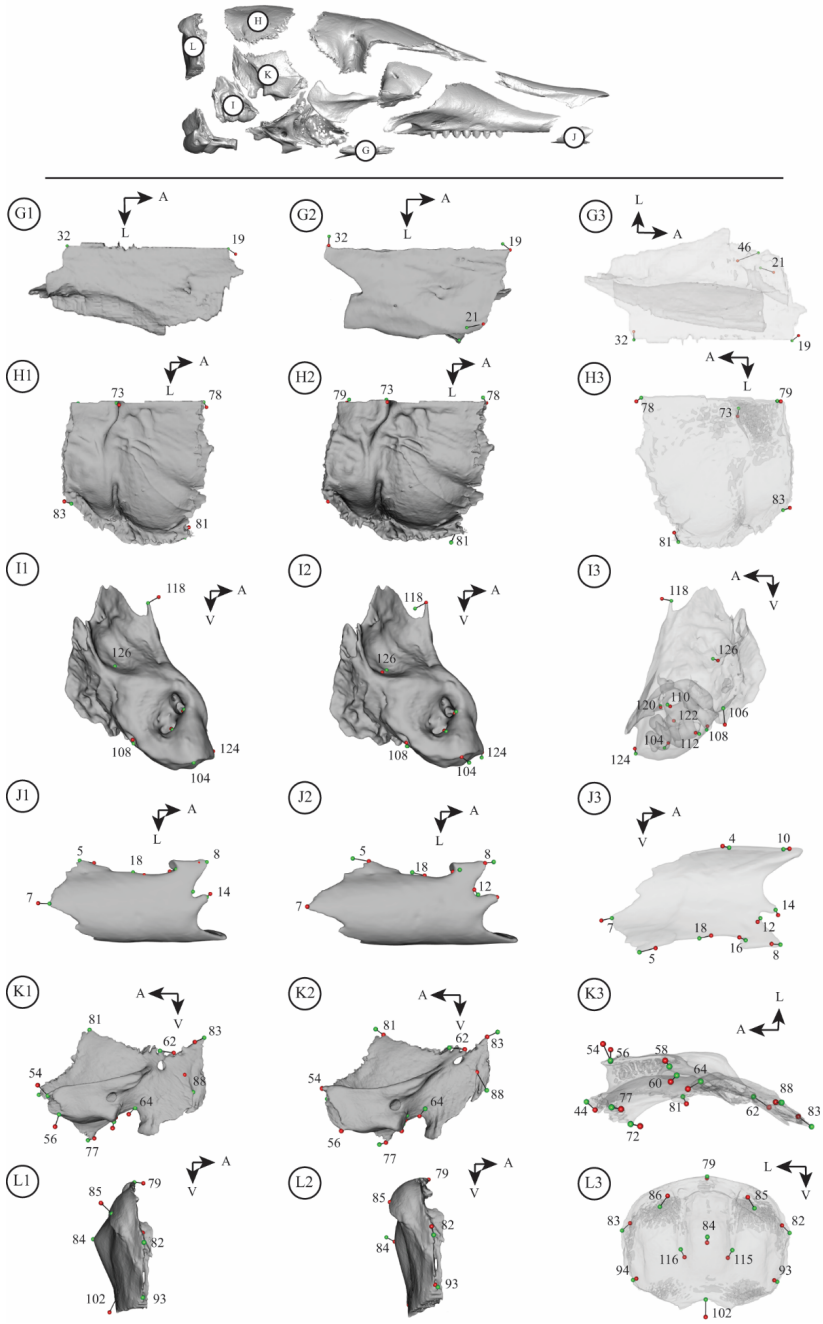

Figure 5. Vector representation of the allometric shape changes detected for a given cranial unit (OBU), represented between its minimal (green – smaller centroid size) and maximal (red – larger centroid size) shapes (see Fig. 2). Results of the analysis performed at the ontogenetic level, and with the log skull centroid size taken as the size variable (see text). For each OBU, the changes are shown in three subsections organized horizontally: 1, vectors from minimal to maximal shape with minimal OBU shape; 2, same as 1) with maximal OBU shape; 3, minimal OBU shape in transparency with vectors. G) palatine; G1-G2, ventral view; G3, dorsal view. H) parietal; H1-H2, ventral view; H3, dorsal view. I) petrosal; I1-I2, medial view; I3, lateral view. J) premaxillary; J1-J2, ventral view; J3, medial view. K) squamosal; K1-K2, lateral view; K3, ventral view. L) supraoccipital; L1-L2, lateral view; L3, occipital view. Landmark numbers and orientation arrows were added for more readability as well as the overall representation of the unpaired bone (supraoccipital). Abbreviations: A, anterior; L, lateral; V, ventral.

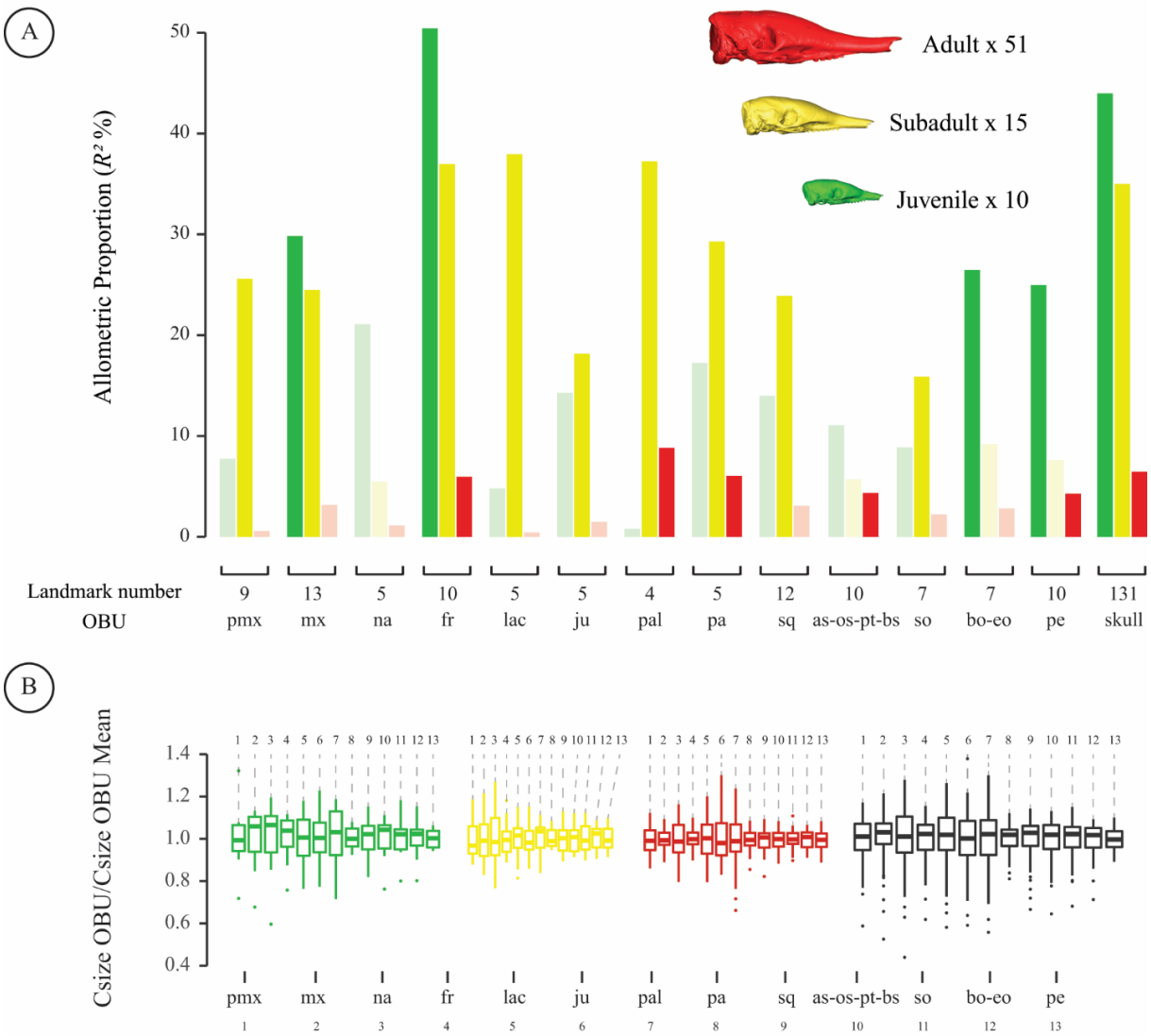

Figure 6. Allometry and growth pattern per cranial unit (OBU) and per postnatal ontogenetic stage. A) Bar graph showing the allometric proportions of shape variation per OBU and ontogenetic stage (see text). OBU caption is found in panel B. Bars with transparency indicate a statistically unsupported allometry for a given OBU and stage (at p value > 0.05) (see Table 4). B) Boxplot showing the variation of size for each OBU relative to its mean per stage (green, juvenile; yellow, subadult; red, adult), and for the whole sample (in black), as measured by the following ratio for every specimen: log OBU centroid size / mean log OBU centroid size at a given stage. Abbreviations of OBUs: as-os-pt-bs, alisphenoid-orbitosphenoid-pterygoid-basisphenoid complex; bo-eo, basioccipital-exoccipital complex; fr, frontal; ju, jugal; lac, lacrimal; mx, maxillary; na, nasal; pa, parietal; pal, palatine; pe, petrosal; pmx, premaxillary; so, supraoccipital; sq, squamosal.

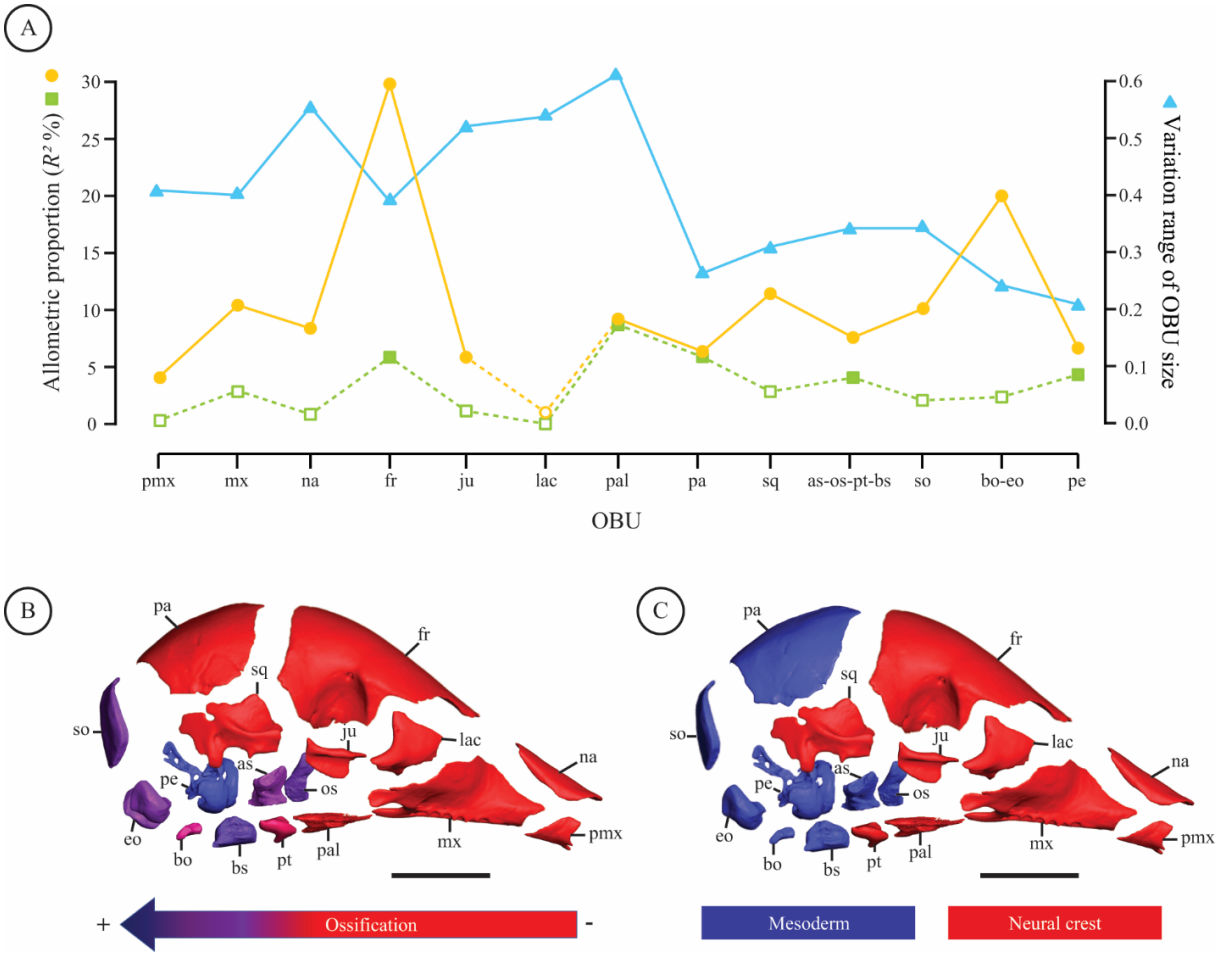

Figure 7. Comparison between the allometric proportion of shape variation, the variation in size and developmental characteristics for each cranial unit treated in this paper (see Discussion). A) Allometric proportions at ontogenetic (light orange circles) and static (light green squares) levels (unfilled figures correspond to non-supported allometric effects, see text) and variation range of each OBU's size around its mean (light blue triangles). The latter is calculated as the interval between the first and third quartile of the ratio used in Fig. 6C, for the whole sample. B) Ossification chain according to Hautier *et al*. (2011). C) Distribution of embryonic origin of each bone according to Piekarski *et al*. (2014). Abbreviations: as-os-pt-bs, alisphenoid-orbitosphenoid-pterygoid-basisphenoid complex; bo-eo, basioccipital-exoccipital complex; fr, frontal; ju, jugal; lac, lacrimal; mx, maxillary; na, nasal; pa, parietal; pal, palatine; pe, petrosal; pmx, premaxillary; so, supraoccipital; sq, squamosal. Scale-bar = 1 cm.

TABLE CAPTIONS

Table 1. Definition of external landmarks. * Suture exoccipital/supraoccipital marks by a bulge in adult.

Number	Definition
1	Most anterodorsal point of the internasal suture
2	Intersection between internasal suture and frontal bone
3-4	Triple contact point between premaxillary/maxillary/nasal
5	Intersection between midline and premaxillary/ maxillary suture
6-7	Most posterior point of the premaxillary/maxillary suture on the palate
8	Most anterior point of the premaxillary midline suture
9-10	Most anterior point of the premaxillary/nasal suture
11-12	Maximum curvature point between #8 and the anterior process of the premaxillary

13-14	Most anterior point of the premaxillary anterior process
15-16	Most anterior point of incisive foramen in strict ventral view
17-18	Most posterior point of incisive foramen in strict ventral view
19	Intersection between palatine/maxillary suture and the palate midline
20-21	Intersection between maxillary/palatine suture and lateral edge of palate
22-23	Intersection between jugal/maxillary suture and ventral edge of zygomatic arch
24-25	Most dorsal point of the maxillary foramen
26-27	Most dorsal point of the infraorbital foramen
28-29	Most anterior point of the alveolar margin of the premolar tooth row
30-31	Most posterior point of the alveolus margin of the premolar tooth row
32	Most posterior point of the palatine midline
33-34	Triple contact point between frontal/maxillary/nasal
35-36	Triple contact point between lacrimal/maxillary/frontal
37-38	Intersection between the lacrimal/frontal suture and the anterieur orbital edge
39-40	Anteroventral margin of the lacrimal foramen
41-42	Most dorsomedial point of the orbit (*i.e.*, minimal interorbital length)
43-44	Triple contact point between squamosal/frontal/alisphenoid
45-46	Most anteroventral point of caudal palatine foramen (in lateral view)
47-48	Most anteroventral point of the sphenorbitaire fissure
49-50	Triple contact point between maxillary/jugal/lacrimal
51-52	Intersection between anterior orbital edge and jugal/lacrimal suture
53-54	Most dorsal point of the jugal/squamosal suture
55-56	Most ventral point of the jugal/squamosal suture
57-58	Most ventral point of the postglenoid process
59-60	Most posterodorsal point of the postglenoid foramen
61-62	Most posterodorsal point of the zygomatic ridge of the squamosal
63-64	Most dorsal point of the external acoustic meatus on squamosal (in lateral view)
65-66	Most posterior point of the small alisphenoid process delimitating the carotid notch laterally
67-68	Most anteroventral point of the transverse canal foramen
69-70	Most anteroventral point of the foramen ovale
71-72	Most posterior point of the alisphenoid/squamosal suture in front of pyriform fenestra
74-75	Most anterodorsal point of the optic foramen
76-77	Ventral tip of entoglenoid process
78	Intersection between frontal/parietal suture and the midline
79	Intersection between parietal/supraoccipital suture and the midline
80-81	Triple contact point between the frontal/squamosal/parietal
82-83	Triple contact point between the parietal/squamosal/supraoccipital
84	Most distal point of the supraoccipital on the midline (occipital face)
85-86	Most posterior point of the nuchal process of the supraoccipital
87-88	Most anterodorsal point of the sulcus for the occipital artery
89-90	Most lateral point of basioccipital/basisphenoid suture
91-92	Intersection between the anteromedial edge of occipital condyle and foramen magnum
93-94	Triple contact point between the supraoccipital/exoccipital/petrosal*
95-96	Most posterolateral point of the jugular foramen
97-98	Most posterolateral point of the hypoglossal foramen
99-100	Most anterolateral point of the occipital condyle (in ventral view)
101	Most anteroventral point of the foramen magnum
102	Most posterodorsal point of the foramen magnum
103-104	Most medial point of promontorium of petrosal in ventral view
105-106	Most anteroventral point of mastoid process (= paroccipital process of petrosal)
107-108	Most ventral point of external aperture of cochlear canaliculus
109-110	Most anterior point of the fenestra vestibuli
111-112	Most anteroventral point of the external apertur of cochlear fossula

Table 2. Definition of internal landmarks. * Landmark removed in 3B analyses. ** Projected landmark.

Number	Definition
73	Anteroventral tip of the tentorial process on the midline
113	Dorsal intersection of annular ridge and midline
114*	Dorsal intersection between cribriform plate and median septum posterior to the latter
115-116	Maximum curvature point of the lateral occipital ridge in caudal cerebral fossa
117-118	Most dorsal point of the petrosal on the level of the crista tentoria transversally
119-120	Most anteromedial point of the foramen acusticum superius
121-122	Most anteromedial point of the foramen acusticum inferius
123-124	Most anterior point of epitympanic wing of petrosal
125-126	Maximum curvature point in the ventromedial area of the fossa subarcuata
127-128	Most dorsal point of the internal posterior aperture of the optic canal

129-130	Most ventromedial point on the annular ridge lateral to posterior median septum
131**	Dorsal projection of the most posterior point of the frontal sinuses in the midline

Table 3. Results of the multivariate regression for ES and 3B with log skull centroid size at the ontogenetic and static levels. Index: *a*, slope coefficient; Intercept; R^2, allometric proportion of shape variation; *p-value*, significance following the permutation test. The shaded lines correspond to the tests with a non-significant *p-value* (> 0.05).

	Log Skull Centroid Size							
	Ontogenetic Level				Static Level			
	a	intercept	R^2	*p-value*	a	intercept	R^2	*p-value*
Entire Skull	0.2273	-2.8776	0.27618	0.0001	0.2307	-2.9312	0.06311	0.0001
Premaxillary	2.6620	-6.7570	0.04242	0.0054	2.3270	-5.9140	0.00558	0.9774
Maxillary	2.5780	-6.5430	0.10665	0.0001	3.2890	-8.3600	0.03148	0.1040
Nasal	1.6900	-4.2890	0.08368	0.0004	1.4820	-3.7670	0.01127	0.6700
Frontal	5.2690	-13.376	0.29873	0.0001	5.1750	-13.155	0.05965	0.0200
Lacrimal	1.8680	-4.7420	0.01568	0.2802	2.4230	-6.1600	0.00429	0.9425
Jugal	3.2730	-8.3090	0.06006	0.0015	3.7490	-9.5290	0.01476	0.5640
Palatine	4.0190	-10.202	0.09004	0.0006	9.7290	-24.730	0.08829	0.0053
Parietal	2.2530	-5.7180	0.06661	0.0005	5.1620	-13.121	0.06036	0.0120
Squamosal	3.7480	-9.5130	0.11490	0.0001	4.6370	-11.787	0.03084	0.0875
As-Os-Pt-Bs	3.8850	-9.8610	0.07351	0.0001	7.4030	-18.819	0.04347	0.0178
Supraoccipital	3.5370	-8.9790	0.10031	0.0001	4.0930	-10.405	0.02223	0.3164
Bo-Eo	4.7010	-11.933	0.19612	0.0001	4.0220	-10.223	0.02801	0.1756
Petrosal	2.6430	-6.7100	0.06281	0.0001	5.5540	-14.119	0.04270	0.0242

Table 4. Results of the multivariate regression for ES and 3B with log skull centroid size for each ontogenetic stage. Index: *a*, slope coefficient; Intercept; *α**, angle of the slope with the horizontal axis in the common allometry analyses; R^2, allometric proportion of the shape variation; *p-value*, significance following the permutation test. The shaded lines correspond to the tests with a non-significant *p-value* (> 0.05).

	Log Skull Centroid Size														
	Juvenile (N = 10)					Subadult (N = 15)					Adult (N = 51)				
	a	intercept	α*	R^2	*p-value*	a	intercept	α*	R^2	*p-value*	a	Intercept	α*	R^2	*p-value*
Entire Skull	0.2842	-3.5343	36.35	0.45026	0.0005	0.3612	-4.5690	40.39	0.34846	0.0002	0.2307	-2.9312	23.09	0.06311	0.0002
Premaxillary	3.5220	-8.8770	40.02	0.07737	0.7393	9.8730	-25.054	40.29	0.25597	0.0016	2.3270	-5.9140	40.13	0.00558	0.9774
Maxillary	3.7910	-9.5550	-39.72	0.29837	0.0053	5.9980	-15.219	-39.18	0.24496	0.0008	3.2890	-8.3600	-15.61	0.03148	0.1040
Nasal	2.8210	-7.1110	-29.81	0.21065	0.1068	1.5110	-3.8350	-29.88	0.05470	0.5587	1.4820	-3.7670	-29.84	0.01127	0.6700
Frontal	6.1710	-15.554	36.87	0.50433	0.0005	8.1520	-20.687	41.51	0.36966	0.0004	5.1750	-13.155	23.50	0.05965	0.0200
Lacrimal	2.5470	-6.4210	0.990	0.04779	0.8327	15.430	-39.150	61.83	0.37951	0.0023	2.4230	-6.1600	-7.180	0.00429	0.9425

Jugal	4.6950	-11.835	37.47	0.14280	0.2647	9.5180	-24.153	37.90	0.18160	0.0394	3.7490	-9.5290	37.41	0.01476	0.5640
Palatine	0.8950	-2.2564	2.570	0.00776	0.9931	12.390	-31.450	23.58	0.37248	0.0031	9.7290	-24.730	-65.62	0.08829	0.0053
Parietal	3.2760	-8.2570	14.13	0.17248	0.1762	6.8370	-17.348	61.72	0.29289	0.0014	5.1620	-13.121	-56.18	0.06036	0.0120
Squamosal	3.7980	-9.5740	29.92	0.13981	0.2253	7.7990	-19.791	50.64	0.23893	0.0006	4.6370	-11.787	27.04	0.03084	0.0875
As-Os-Pt-Bs	4.0700	-10.260	27.29	0.11073	0.4488	4.5870	-11.639	27.35	0.05703	0.6605	7.4030	-18.819	27.66	0.04347	0.0178
Supraoccipital	2.7750	-6.9940	31.53	0.08856	0.5530	6.2200	-15.780	31.48	0.15893	0.0421	4.0930	-10.405	31.40	0.02223	0.3164
Bo-Eo	4.3580	-10.986	28.50	0.26473	0.0124	4.0810	-10.356	28.77	0.09176	0.2475	4.0220	-10.223	28.64	0.02801	0.1756
Petrosal	4.4010	-11.093	39.49	0.24980	0.0071	4.1190	-10.452	39.61	0.07592	0.3881	5.5540	-14.119	39.45	0.04270	0.0242

SUPPORTING INFORMATION

Supplementary Information 1. Protocol and results of the determination of ontogenetic stages.

Supplementary Information 2. Description of allometric variations of OBUs at the static level. Only OBUs with statistically supported allometric variation are discussed in this document.

Figure S1. CT-scan sections representing the five dental stages defined in relation to the eruption of deciduous (dPM) and permanent teeth (PM). The analysed locus always corresponds to the 4th premolar represented here by an arrow. Based on our observations of the upper dentition, we defined five dental stages: (1) dPMs starting to mineralize or erupting; (2) all dPMs well mineralized, possibly all erupted, no PM in the crypts (i.e., PM not mineralized); (3) all dPMs erupted, with part of the PMs mineralized but still in the crypts (not yet reaching the alveoli); (4) part of the dPMs about to be replaced by PMs (one or several PMs has/have erupted through the alveoli, but remain(s) almost unworn); (5) all PMs erupted and no remain of dPMs left (see Supplementary Information 1).

Figure S2. Bivariate linear regressions among three dentary measurements and the LTC. A. With the height of the P4/dPM4. B. With the height of the alveoli of the PM4/dPM4. C. With the height of the growth front of the P4/dPM4. Each measurement is illustrated in the section to the right of each graph. For each simple regression, the slope equation, R^2, significance of the *t-test* and significance of the *F-test* are specified. In each case, specimens, whose dental stage (2 or 5) is unknown, were determined *a posteriori* (see Supplementary Information 1).

Figure S3. Ontogenetic stages determined based on dental eruption, as compared to the ossification score and the total length of the skull (LTC). The dental stages correspond here to: 1, stillborn (n = 1); 2, juvenile (n = 11); 3, subadult 1 (n = 7); 4, subadult 2 (n = 9); 5, adult (n = 56). The black dots refer to specimens (n = 12) whose dental stage could not be determined. See Supplementary Information 1 for more detail.

Figure S4. Allometric trajectories among three nine-banded armadillo's morphotypes (Southern, Central and Northern) at ontogenetic (A – illustrated by juvenile and adult specimens in dorsal view) and static (B – illustrated by adult specimens in dorsal view) levels. The y-axis values are the principal component 1 of the predicted values of a multivariate regression of shape on size; the x-axis values are the log-transformed skull centroid sizes for each specimen. For each level, the HOS test, Procrustes ANOVA and Pairwise comparisons of the allometric trajectory angles results are shown (in bold, the R^2 and *p-value* for the first two analyses and the angles between the slope and its intercept with a significant *p-value*). Scale bar: 1 cm. (see Material and Methods).

Figure S5. Vector representation in southern morphotype of the allometric shape changes detected for the entire skull and a given cranial unit (OBU), represented between its minimal (green – smaller centroid size) and maximal (red – larger centroid size) shape (see Fig. 2) with the associated R^2 and *p-value*. Results of the analyses performed at the ontogenetic level, and with the log skull centroid size taken as the size variable (see text). For each OBU, the changes are shown in one view with vectors from minimal to maximal shape with the minimal OBU shape shown in transparency. A) Entire skull in dorsal view. B) Entire skull in lateral view. C) Alisphenoid-orbitosphenoid-pterygoid-basisphenoid complex in dorsal view. D) Basioccipital-exoccipital complex in ventral view. E) Frontal in ventral view. F) Jugal in medial view. G) Maxillary in medial view. H) Nasal in ventral view. I) Palatine in dorsal view. J) Parietal in dorsal view. K) Petrosal in lateral view. L) Premaxillary in medial view. M) Squamosal in ventral view. N) Supraoccipital in occipital view. Landmark numbers and orientation arrows were added for more readability as well as the overall representation of the unpaired bones (basioccipital and supraoccipital). Abbreviations: A, anterior; D, dorsal; L, lateral; V, ventral.

Figure S6. Multivariate regression for each OBU at the ontogenetic level using log skull centroid size.

Figure S7. Multivariate regression for each OBU at the static level with log skull centroid size.

Figure S8. Vector representation of the allometric shape changes detected for a given cranial unit (OBU), represented between its minimal (green – smaller centroid size) and maximal (red – larger centroid size) shape (see Fig. 2). Results of the analysis performed at the static level,

and with the log skull centroid size as the size variable (see text). For each OBU, the changes are shown in three subsections organized horizontally: 1, vectors from minimal to maximal shape with minimal OBU shape; 2, same as 1) with maximal OBU shape; 3, minimal OBU shape in transparency with vectors. A) Alisphenoid-orbitosphenoid-pterygoid-basisphenoid complex; A1-A2, dorsal view; A3, lateral view. B) Frontal; B1-B2, ventral view; B3, lateral view. C) Palatine; C1-C2, dorsal view; C3, ventral view. D) Parietal; D1-D2, dorsal view; D3, ventral view. Landmark numbers and orientation arrows were added for more readability. Abbreviations: A, anterior; D, dorsal; L, lateral.

Figure S9. Common allometric analyses. Trajectories are derived from homogeneity of slope test, plotting log transformed geometric means in the x-axis (i.e., log skull centroid size) and the PC1 of the predicted values of multivariate regression of shape ratios on size in the y-axis (Shape (Predicted)) (see Material and Methods).

Table S1. List of specimens.

Table S2. Landmark coordinates without treatment.

Table S3. List of landmarks placed on each of the 76 specimens, with a precision on the estimated landmarks (in red) (see Material and Methods).

Table S4. Measurements on the location of the P4, LTC and dental stages. * Specimen assigned to a dental stage *a posteriori* (see Fig. S2).

Table S5. Ontogenetic table with the ossification score, the dental score and LTC.

1286

1287 Table S6. Statistical results of the Procrustes ANOVA from the multivariate regressions at
1288 ontogenetic and static level for ES and 3B analyses with log skull centroid size (see Table 3).

1289

1290 Table S7. Statistical results of the Procrustes ANOVA from the multivariate regressions for
1291 each ontogenetic stage for 3B approach using the log skull centroid size (see Table S4).

1292

1293 Table S8. Statistical results of the homogeneity of slope test between ontogenetic stages using
1294 the log skull centroid size (see Fig. S9). A significant *p-value* (< 0.05 – unshaded line) implies
1295 that at least one of the groups has a different allometric trajectory from the others.